Thesis for the degree of Doctor of Philosophy

Runaway Electrons and Alfvén Eigenmodes in Tokamaks

Håkan Smith

CHALMERS

Department of Radio and Space Science
Chalmers University of Technology
Göteborg, Sweden, 2006

Runaway Electrons and Alfvén Eigenmodes in Tokamaks
Håkan Smith

ISBN 91-7291-857-8
Doktorsavhandlingar vid Chalmers tekniska högskola
Ny serie nr 2539
ISSN 0346-718X

Department of Radio and Space Science
School of Electrical Engineering
Chalmers University of Technology
SE–412 96 Göteborg
Sweden
Telephone +46–(0)31–772 10 00

Printed in Sweden by
Reproservice
Chalmers Tekniska Högskola
Göteborg, Sweden, 2006

Runaway Electrons and Alfvén Eigenmodes in Tokamaks
Håkan Smith
Department of Radio and Space Science
Chalmers University of Technology

Abstract

Runaway electrons can be generated during fusion experiments as a consequence of the rapid thermal quench of the plasma in a tokamak disruption. If the time scale of this cooling is short compared to the collision time in the tail of the electron velocity distribution, incomplete thermalisation of this tail leads to a burst of runaway production. This phenomenon is investigated in the present thesis and simple criteria for whether it produces more runaways than the ordinary Dreicer runaway generation mechanism are derived.

In tokamak disruptions a large part of the pre-disruption Ohmic current can be converted into a runaway current. A simple model for the current dynamics is presented and analysed analytically and numerically. The radial profile of the runaway current is found to become significantly more peaked on the magnetic axis than the pre-disruption profile in tokamaks with a large current.

Furthermore, the effects of synchrotron radiation in the high energy runaway tail of the steady-state electron distribution function are studied and the governing kinetic equation is found to be of a two-way diffusion form. A general analytic scheme for solving two-way diffusion equations is developed.

The theory of localisation of compressional Alfvén eigenmodes to the edge of a tokamak plasma is extended to the case of spherical tokamaks, which have elliptic cross section and aspect ratio of order unity. Another theory is developed in order to explain experimentally observed second harmonic density perturbations of Alfvén cascade eigenmodes. The second harmonic perturbation is generated as a nonlinear sideband of the Alfvén cascade through quadratic terms in the magnetohydrodynamic equations.

Keywords: fusion plasma physics, runaway electron, tokamak disruption, two-way diffusion equation, compressional Alfvén eigenmode, Alfvén cascade

Publications

This thesis is based on the work contained in the following papers:

[A] P. Helander, H. Smith, T. Fülöp, and L.-G. Eriksson, "Electron kinetics in a cooling plasma", Physics of Plasmas **11**, 5704 (2004).

[B] H. Smith, P. Helander, L.-G. Eriksson, and T. Fülöp, "Runaway electron generation in a cooling plasma", Physics of Plasmas **12**, 122505 (2005).

[C] H. Smith, P. Helander, L.-G. Eriksson, D. Anderson, M. Lisak, and F. Andersson, "Runaway electrons and the evolution of the plasma current in tokamak disruptions", Physics of Plasmas **13**, 102502 (2006).

[D] F. Andersson, P. Helander, D. Anderson, H. Smith, and M. Lisak, "Approximate solutions of two-way diffusion equations", Physical Review E **65**, 036502 (2002).

[E] F. Andersson, H. Smith, D. Anderson, P. Helander, and M. Lisak, "Effects of Backscattering on One-Dimensional Electron Beam Transport", Nuclear Science and Engineering **142**, 150 (2002).

[F] H. Smith, T. Fülöp, M. Lisak, and D. Anderson, "Localization of compressional Alfvén eigenmodes in spherical tori", Physics of Plasmas **10**, 1437 (2003).

[G] H. Smith, B. N. Breizman, M. Lisak, and D. Anderson, "Nonlinearly driven second harmonics of Alfvén cascades", Physics of Plasmas **13**, 042504 (2006).

Conference contributions (not included in the thesis)

H. Smith, T. Fülöp, M. Lisak, and D. Anderson, "Localization of fast magnetosonic eigenmodes in spherical tori", 29th EPS Conference on Plasma Physics and Controlled Fusion, Montreux (2002), P4.115.

H. Smith, T. Fülöp, M. Lisak, and D. Anderson, "Localization of compressional Alfvén eigenmodes in spherical tori", Annual Meeting of the Swedish Fusion Research Unit, Göteborg (2002).

H. Smith, P. Helander, and T. Fülöp, "Runaway electron generation in a cooling plasma", Annual Meeting of the Swedish Fusion Research Unit, Studsvik (2004).

H. Smith, P. Helander, and T. Fülöp, "Runaway electron generation in a cooling plasma", 31st EPS Conference on Plasma Physics, London (2004), P5.194.

P. Helander, F. Andersson, L.-G. Eriksson, T. Fülöp, H. Smith, D. Anderson, and M. Lisak, "Runaway electron generation in tokamak disruptions", 20th IAEA Fusion Energy Conference, Vilamoura (2004), TH/P4-39.

H. Smith, P. Helander, and T. Fülöp, "Runaway electron generation in a cooling plasma", 46th Annual Meeting of the APS Division of Plasma Physics, Savannah (2004), CP1.034.

H. Smith, B. N. Breizman, M. Lisak, and D. Anderson, "Nonlinearly driven second harmonics of Alfvén Cascades", 32nd EPS Plasma Physics Conference, Tarragona (2005), P4.121.

H. Smith, B. N. Breizman, M. Lisak, and D. Anderson, "Nonlinearly driven second harmonics of Alfvén Cascades", 9th IAEA Technical Meeting on Energetic Particles in Magnetic Confinement Systems, Takayama (2005), OT01.

H. Smith, P. Helander, L.-G. Eriksson, D. Anderson, M. Lisak, and F. Andersson, "Runaway electrons and the evolution of the plasma current in tokamak disruptions", 33rd EPS Plasma Physics Conference, Rome (2006), P4.178.

K. Gál, H. Smith, T. Fülöp, and P. Helander, "Runaway electron generation during plasma shutdown by killer pellet injection", 21st IAEA Fusion Energy Conference, Chengdu (2006), TH/P3-2.

M. Porkolab, E. Edlund, L. Lin, R. Parker, C. Rost, J. Sears, J. Snipes, S. J. Wukitch, B. N. Breizman, N. N. Gorelenkov, G. J. Kramer, A. Fasoli, H. Smith, "Experimental studies and analysis of Alfvén eigenmodes in Alcator C-Mod", 21st IAEA Fusion Energy Conference, Chengdu (2006), EX/P6-16.

Contents

Acknowledgements

I want to thank my supervisors Dr. Tünde Fülöp, Prof. Dan Anderson, and Prof. Mietek Lisak for their guidance, encouragement, and for creating an inspiring atmosphere in the group. A special thanks goes to Prof. Per Helander, for all his help and support during my runaway electron studies. I also want to thank Dr. Fredrik Andersson and Dr. Lars-Göran Eriksson for a fruitful collaboration in connection to runaway electrons, and Prof. Boris Breizman for guiding me through the Alfvén cascade problem. I am grateful to Dr. Pontus Johannisson and Dr. Ulf Jordan especially for computer support, Monica Hansen-Torvaldsson for helping me with various practical matters, and all the people in the Nonlinear Electrodynamics group for being such friendly colleagues. Last but not least, I wish to thank my parents and family for being there for me, and my best beloved Tove Wiklund for her love and support.

Abbreviations

Tokamaks and their locations

Alcator C-Mod	The modified Alto Campo Torus C, Massachusetts Institute of Technology, Cambridge, USA.
DIII-D	The Doublet III with D-shaped plasma, General Atomics, San Diego, USA.
ITER	The International Thermonuclear Experimental Reactor, to be built in Cadarache, France.
JET	The Joint European Torus, Culham Science Centre, Abingdon, United Kingdom.
JT-60U	The Japan Atomic Energy Research Institute Tokamak-60 Upgrade, Naka, Japan.
MAST	The Mega Ampere Spherical Tokamak, Culham Science Centre, Abingdon, United Kingdom.
NSTX	National Spherical Tokamak Experiment, Princeton Plasma Physics Laboratory, USA.
TFTR	The Tokamak Fusion Test Reactor, Princeton Plasma Physics Laboratory, USA (1982-1997).

Other acronyms

AC	Alfvén Cascade
CAE	Compressional Alfvén eigenmode
EPM	Energetic particle mode
GAE	Global shear Alfvén eigenmode
ICE	Ion cyclotron emission
ICRH	Ion cyclotron resonance heating
MHD	Magnetohydrodynamic(s)

NBI	Neutral beam injection
RSAE	Reversed shear Alfvén eigenmode, synonym to AC
TAE	Toroidicity induced Alfvén eigenmode
VDE	Vertical displacement event

Chapter 1

Introduction

As the world population grows, the increasing demand for energy poses a major challenge to the scientific community. Fusion is the way the sun and other stars produce energy, and if we could use the same process on Earth, we would have a clean, safe, and virtually inexhaustible way to meet the increasing energy demand.

Fusion of the two hydrogen isotopes deuterium (D) and tritium (T) leads to the formation of an alpha particle and a neutron in the reaction

$$\mathrm{D}^+ + \mathrm{T}^+ \longrightarrow {}^4\mathrm{He}^{2+}\ (3.5\ \mathrm{MeV}) + \mathrm{n}\ \ (14.1\ \mathrm{MeV}),$$

where a large amount of energy is released due to the mass difference between the products and the reactants. To make the D and T particles fuse, they have to come close enough for the nuclear forces to overcome the electric Coulomb repulsion. One way to achieve this is to have a D–T plasma with very high temperature (around 100 MK), so that the thermal energy makes it possible for the particles to pass the potential barrier. This process is called thermonuclear fusion.

The sun is held together by its gravity, but a fusion plasma on Earth has to be confined by other means, and one way to solve this problem is magnetic confinement. When a static magnetic field is present in a plasma the charged particles will gyrate around the magnetic field lines. This confines them in the direction perpendicular to the field, and to confine them also in the parallel direction the magnetic field lines can be bent into a torus.

The most promising torus shaped confinement configuration in fusion research today is the *tokamak* [1], which is symmetric around the major axis of the torus. The word tokamak is a Russian acronym for

тороидальная камера с магнитными катушками.[1] To average out deconfining particle drifts induced by the bending of the magnetic field lines the tokamak plasma has to carry a toroidal current which produces a poloidal magnetic field component.

To achieve a large output power from the fusion reactions the plasma density and the temperature have to be high and the confinement time has to be long. In addition, an *ignited* plasma must be self-sustaining, which means that the deuterium and tritium ions have to be heated effectively by the internal plasma processes only, i.e. by the fusion generated 3.5 MeV alpha particles. If the alpha particle heating power is not enough to maintain the high temperature, the plasma will not be ignited, and the process has to be driven by external heating. The neutrons produced in the fusion reactions are not confined by the magnetic field, so they leave the plasma and their energy is converted into heat. This heat is the energy that could be converted to electricity in a fusion power plant.

The largest currently existing fusion experiment is the Joint European Torus (JET) tokamak situated in Culham, UK. It holds the world record from 1997 of 16.1 MW produced D–T fusion power during one second [2]. The next step towards demonstrating the feasibility of fusion as an energy source is the planned International Thermonuclear Experimental Reactor (ITER), which will be built in Cadarache, France. ITER is designed to produce more energy than it consumes and will demonstrate alpha particle heating.

Different kinds of instabilities pose a major difficulty in tokamak confinement. Large scale magnetohydrodynamic instabilities can deteriorate the plasma confinement in different ways, sometimes leading to plasma disruptions. Disruptions may result in generation of very fast "runaway electrons", which is one of the main topics of this thesis. The other topic is Alfvén eigenmodes, which may be driven unstable by wave–particle interaction. These instabilities do not usually lead to violent events like disruptions, but they can cause a redistribution of particles or energy, and thereby affect the confinement time.

The friction force on an electron is mainly caused by collisions with other electrons, and it increases with velocity for electrons of moderate energy. For energetic electrons however, the friction force decreases with increasing velocity. If an electric field is present in the plasma, electrons

[1] toroidal'naya kamera s magnitnymi katushkami—toroidal chamber with magnetic coils.

above a certain velocity experience an electric force that is stronger than the friction force, and they will be accelerated to very high velocities. These electrons are called runaway electrons, since they leave the thermal population of electrons.

When a plasma instability leads to a disruption in a tokamak, the plasma interacts with the wall and the temperature falls rapidly. The resistivity rises dramatically, but the plasma maintains its current through the induction of a large electric field. If this electric field is above a certain critical electric field, runaway electrons will be produced, which replace a large part of the initial current. Loss of runaway electrons to the wall of the tokamak may cause severe localised surface damage. Runaway electron generation and its effect on the current distribution in disruptions are important topics that are discussed in this thesis.

External heating of the plasma and fusion reactions can produce a population of fast ions (not as fast as the runaway electrons, though). The resulting deviation of the ion distribution function from thermodynamic equilibrium constitutes a source of energy for different plasma waves. Alfvén waves[2] may be excited by resonant interaction with energetic ions, and much research has been devoted to describing these instabilities.

Radiation from compressional Alfvén eigenmodes (CAEs) excited by superthermal ions has been observed in different tokamaks, and it has previously been shown that these eigenmodes are localised to the outboard side of the torus. This thesis extends the theory of localisation of CAEs to the case of a spherical tokamak, where the plasma cross section has a large ellipticity and the plasma radius is of the same order as the major radius of the torus.

Alfvén Cascades (ACs) are another type of eigenmodes, which are not only excited by the fast ion population, but also rely on the non-perturbative effect of these ions for the existence of a stable mode structure. ACs are useful for diagnosing the current distribution in a tokamak and have been found to closely correlate with the triggering of internal transport barriers. In this thesis a theory for non-linear generation of a second harmonic of the AC is developed.

The thesis is organised as follows: Chapter 2 introduces the Fokker-Planck kinetic equation and the runaway electron phenomenon. Chapter 3 describes how runaway electron generation is affected if the cooling

[2]Alfvén waves are named after Hannes Alfvén, who received the Nobel Prize in physics 1970 and was the nephew of the famous Swedish composer Hugo Alfvén.

time of the plasma is comparable to the collision time in the tail of the electron distribution. The evolution of the radial profiles of the electric field and the runaway electron density during a tokamak disruption is studied in Chapter 4. In Chapter 5 a general theory for two-way diffusion equations is developed. It is used to study the kinetics of electron scattering and the steady-state distribution of high energy runaway electrons. Chapter 6 describes the basic theory of Alfvén eigenmodes. The radial and poloidal localisation of compressional Alfvén eigenmodes in a spherical tokamak is discussed in Chapter 7. Chapter 8 deals with nonlinearly generated second harmonics of Alfvén cascade eigenmodes. Finally, the main conclusions of the thesis are presented in Chapter 9.

Chapter 2

Runaway electrons

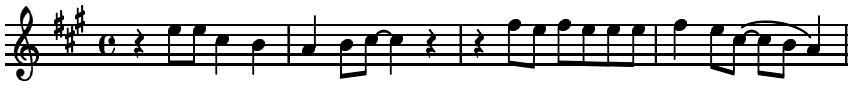

—Runaway, D. Shannon, M. Crook

The kinetic equation, which describes particle dynamics in a plasma, is the starting point of this chapter. Then the effects of Coulomb collisions and how these are modelled by the Fokker-Planck collision operator are studied. From this theory, the friction force on fast electrons is shown to decrease as the velocity increases. The non-monotonic velocity dependence of the friction force gives rise to the runaway electron phenomenon. Runaway electrons can be produced in tokamak disruptions, due to the very high induced electric field. In a magnetised plasma, synchrotron radiation counteracts the acceleration of runaway electrons at ultra-relativistic energies. The appropriate kinetic equation and a simplified picture of the momentum space dynamics are presented at the end of the chapter.

2.1 The kinetic equation

The kinetic theory describes the dynamics of a particle distribution and forms the basis for all understanding of plasma physics. The distribution function of particle species a in space and velocity-space, $f_a(\mathbf{x}, \mathbf{v}, t)$, has to obey an equation essentially expressing particle conservation

$$\frac{\partial f_a}{\partial t} + \frac{\partial}{\partial \mathbf{x}} \cdot (\mathbf{v} f_a) + \frac{\partial}{\partial \mathbf{v}} \cdot (\mathbf{a} f_a) = 0. \tag{2.1}$$

When the acceleration **a** is due to electric and magnetic forces, Eq. (2.1) takes the form of the Vlasov kinetic equation

$$\frac{\partial f_a}{\partial t} + \mathbf{v} \cdot \nabla f_a + \frac{q_a}{m_a}(\mathbf{E} + \mathbf{v} \times \mathbf{B}) \cdot \frac{\partial f_a}{\partial \mathbf{v}} = 0, \tag{2.2}$$

where q_a and m_a are the particle charge and mass, respectively. Close to an individual particle, on short distances compared to the Debye length, the electric and magnetic fields are not simply the macroscopic background fields; a significant contribution to the fields also comes from the particle itself. However, to make a macroscopic description of the plasma, **E** and **B** has to be regarded as the large-scale average fields. The small scale electromagnetic effects, due to short range interaction between particles, are therefore treated separately in the so-called collision operator $\mathcal{C}_a(f)$, which is moved to the right-hand side of the kinetic equation,

$$\frac{\partial f_a}{\partial t} + \mathbf{v} \cdot \nabla f_a + \frac{q_a}{m_a}(\mathbf{E} + \mathbf{v} \times \mathbf{B}) \cdot \frac{\partial f_a}{\partial \mathbf{v}} = \mathcal{C}_a(f_a). \tag{2.3}$$

2.2 Coulomb collisions

Let us consider an elastic Coulomb collision between an electron and an ion, in order to obtain the fundamental scalings of the collision frequency ν_{ei}. The derivation here follows the presentation in Ref. [3]. The ion is heavy compared to the electron, and will not move significantly during the collision. Consequently, the electron velocity vector will essentially only change direction and not magnitude. The situation is shown in Fig. (2.1). The electron is assumed to pass the stationary ion at a distance b, called the impact parameter, which for most collisions is so large that the electron is deflected by only a small angle α from its original direction. Thus, it can be considered to travel approximately in a straight line with speed v, and the distance to the ion is $r(t) \simeq (b^2 + v^2t^2)^{1/2}$ at time t.

The Coulomb force $q_{\mathrm{i}}e/4\pi\epsilon_0 r^2(t)$ gives the electron an impulse perpendicular to its original velocity

$$m_{\mathrm{e}}\Delta v_\perp = \int_{-\infty}^{\infty} \frac{q_{\mathrm{i}}e}{4\pi\epsilon_0 r^2(t)} \frac{b}{r(t)} dt = \frac{q_{\mathrm{i}}e}{2\pi\epsilon_0 bv} \tag{2.4}$$

Since v is typically of the order of the electron thermal velocity $v = v_{T\mathrm{e}}$,

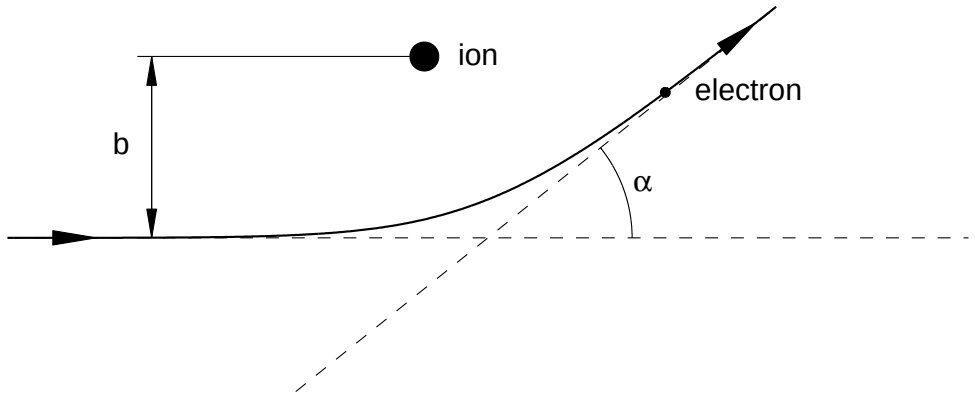

Figure 2.1: Coulomb collision between an electron and an ion.

the deflection angle becomes

$$\alpha = \frac{\Delta v_\perp}{v} = \frac{q_\mathrm{i} e}{2\pi\epsilon_0 m_\mathrm{e} v_{T\mathrm{e}}^2 b} \equiv \frac{b_0}{b}. \tag{2.5}$$

The approximation of the electron orbit as a straight line is justified if $b \gg b_0$, since this gives a small angle of deflection. The typical electron-ion impact parameter is of the order of the Debye length

$$\lambda_\mathrm{D} = \sqrt{\frac{\epsilon_0 T}{n e^2}}, \tag{2.6}$$

because electrons with $b \gg \lambda_\mathrm{D}$ are shielded from the ion by the surrounding plasma. Thus, if $\Lambda \equiv \lambda_\mathrm{D}/b_0 \gg 1$, most collisions will result in only small-angle deflections. In a tokamak plasma, the Coulomb logarithm is around $\ln\Lambda \simeq 17$, so most collisions will indeed give rise to small deflections.

The collision frequency ν_ei is defined so that $1/\nu_\mathrm{ei}$ is the time after which many small-angle deflections have accumulated to cause a significant (say, 90-degree) scattering of the pitch-angle. The direction of the velocity vector $\mathbf{v}$ undergoes a random walk with the small step size angle α and some step frequency ν. The general estimate for a diffusion coefficient is the step frequency times the step size squared. Here, collisions with different α occur with different frequencies ν, so we integrate to get the total diffusion coefficient ν_ei

$$\nu_\mathrm{ei} \sim \int \alpha^2 d\nu. \tag{2.7}$$

The number of ions that an electron passes per unit time at a distance between b and $b + db$ is $d\nu = n_\mathrm{i} v_{T\mathrm{e}} 2\pi b db$, which in view of Eq. (2.5)

yields

$$\nu_{\mathrm{ei}} \sim \int_{b_0}^{\lambda_{\mathrm{D}}} \left(\frac{b_0}{b}\right)^2 n_{\mathrm{i}} v_{T\mathrm{e}} 2\pi b\, db = \left(\frac{q_{\mathrm{i}} e}{\epsilon_0 m_{\mathrm{e}}}\right)^2 \frac{n_{\mathrm{i}} \ln\Lambda}{2\pi v_{T\mathrm{e}}^3}. \tag{2.8}$$

The integral has been cut off at $b = b_0$ to preserve the small angle deflection property, and at $b = \lambda_{\mathrm{D}}$ because of the shielding effect. This truncation gives an inherent uncertainty in all collision frequencies.

2.3 The Fokker-Planck collision operator

The collision operator for a particle species a is generally a sum of contributions $\mathcal{C}_{ab}$ from collisions with particles of all the species b present in the plasma, including $b = a$,

$$\mathcal{C}_a(f_a) = \sum_b \mathcal{C}_{ab}(f_a, f_b). \tag{2.9}$$

A more elaborate analysis than the one in the previous section, including also a non-zero velocity of species b, makes it possible to write the Fokker-Planck collision operator in tensor notation as

$$\mathcal{C}_{ab}(f_a, f_b) = \ln\Lambda \left(\frac{q_a q_b}{m_a \epsilon_0}\right)^2 \frac{\partial}{\partial v_k}\left(\frac{m_a}{m_b}\frac{\partial \varphi_b}{\partial v_k} f_a - \frac{\partial^2 \psi_b}{\partial v_k \partial v_l}\frac{\partial f_a}{\partial v_l}\right), \tag{2.10}$$

where the so-called Rosenbluth potentials [4], are defined as

$$\varphi_b(\mathbf{v}) = -\frac{1}{4\pi}\int \frac{f_b(\mathbf{v}')}{|\mathbf{v}-\mathbf{v}'|} d^3v', \tag{2.11}$$

$$\psi_b(\mathbf{v}) = -\frac{1}{8\pi}\int |\mathbf{v}-\mathbf{v}'| f_b(\mathbf{v}') d^3v'. \tag{2.12}$$

In the case f_b is a Maxwellian distribution

$$f_b(\mathbf{v}) = f_{\mathrm{M}b}(v) \equiv \frac{n_b}{\pi^{3/2} v_{Tb}^3} e^{-(v/v_{Tb})^2}, \tag{2.13}$$

it can be shown that the collision operator (2.10) becomes

$$\mathcal{C}_{ab}(f_a, f_{\mathrm{M}b}) = \nu_{\mathrm{d}}^{ab}\mathcal{L}(f_a) + \frac{1}{v^2}\frac{\partial}{\partial v} v^3 \left[\frac{m_a}{m_a+m_b}\nu_s^{ab} f_a + \frac{1}{2}\nu_{\parallel}^{ab} v \frac{\partial f_a}{\partial v}\right], \tag{2.14}$$

where $\mathcal{L}$ is the Lorentz scattering operator

$$\mathcal{L}(f) \equiv \frac{1}{2}\left[\frac{1}{\sin\theta}\frac{\partial}{\partial\theta}\left(\sin\theta\frac{\partial f}{\partial\theta}\right) + \frac{1}{\sin^2\theta}\frac{\partial^2 f}{\partial\varphi^2}\right] \tag{2.15}$$

expressed in the spherical coordinates of velocity space v, θ, and φ. Often the distribution function is uniform in the azimuthal angle φ, so the last term can be ignored.

In Eq. (2.14), three different collision frequencies have been introduced. The slowing-down frequency ν_{s}^{ab} determines the average rate of deceleration due to collisions with particles of species b. The deflection frequency ν_{d}^{ab} describes how quickly the direction of the velocity vector changes, and $\nu_{\parallel}^{ab}$ is the parallel velocity diffusion coefficient. Denoting $x_s = v/v_{Ts}$, these frequencies are

$$\nu_{\mathrm{d}}^{ab}(v) \equiv \frac{\left\langle (\Delta v_\perp / v)^2 \right\rangle^{ab}}{2\Delta t} = \hat{\nu}_{ab} \frac{\mathrm{erf}(x_b) - G(x_b)}{x_a^3}, \tag{2.16}$$

$$\nu_{\mathrm{s}}^{ab}(v) \equiv -\frac{\left\langle \Delta v_\parallel / v \right\rangle^{ab}}{\Delta t} = \hat{\nu}_{ab} \frac{2T_a}{T_b} \left(1 + \frac{m_b}{m_a}\right) \frac{G(x_b)}{x_a}, \tag{2.17}$$

$$\nu_{\parallel}^{ab}(v) \equiv \frac{\left\langle (\Delta v_\parallel / v)^2 \right\rangle^{ab}}{\Delta t} = \hat{\nu}_{ab} \frac{2G(x_b)}{x_a^3}, \tag{2.18}$$

where the basic collision frequency $\hat{\nu}_{ab}$ is given by

$$\hat{\nu}_{ab} = \frac{n_b q_a^2 q_b^2 \ln \Lambda}{4\pi \epsilon_0^2 m_a^2 v_{Ta}^3}. \tag{2.19}$$

The brackets $\langle \cdot \rangle$ denote statistical averaging, and the parallel ($_\parallel$) and perpendicular ($_\perp$) subscripts refer to the initial direction of the velocity of the colliding particle. $G(x)$ is the Chandrasekhar function (shown in Fig. 2.2):

$$G(x) \equiv \frac{\mathrm{erf}(x) - x\,\mathrm{erf}'(x)}{2x^2} \to \begin{cases} \frac{2x}{3\sqrt{\pi}}, & x \to 0 \\ \frac{1}{2x^2}, & x \to \infty, \end{cases} \tag{2.20}$$

with the error function defined as

$$\mathrm{erf}(x) \equiv \frac{2}{\sqrt{\pi}} \int_0^x e^{-y^2} dy. \tag{2.21}$$

For electrons colliding with ions, regarding the ions as stationary is equivalent to taking the limit $v/v_{T\mathrm{i}} \to \infty$. This makes $\nu_{\mathrm{s}}^{\mathrm{ei}}$ and $\nu_{\parallel}^{\mathrm{ei}}$ vanish, and there remains only the deflection frequency $\nu_{\mathrm{d}}^{\mathrm{ei}}$, which was roughly estimated in the previous section, cf. Eq. (2.8). Here it can be derived from Eq. (2.16) as

$$\nu_{\mathrm{d}}^{\mathrm{ei}}(v_{T\mathrm{e}}) \simeq \hat{\nu}_{\mathrm{ei}} = \frac{n_{\mathrm{i}} e^2 q_{\mathrm{i}}^2 \ln \Lambda}{4\pi \epsilon_0^2 m_{\mathrm{e}}^2 v_{T\mathrm{e}}^3}. \tag{2.22}$$

For electrons colliding with electrons, the collision operator (2.10) becomes non-linear. Nevertheless, if the electron velocity distribution is nearly Maxwellian $f_\mathrm{e} = f_\mathrm{Me} + f_\mathrm{1e}$, the Fokker-Planck operator can be linearised to $\mathcal{C}_\mathrm{ee}(f_\mathrm{e}, f_\mathrm{e}) \simeq \mathcal{C}_\mathrm{ee}(f_\mathrm{1e}, f_\mathrm{Me}) + \mathcal{C}_\mathrm{ee}(f_\mathrm{Me}, f_\mathrm{1e})$, where the second term is negligible, so Eq. (2.14) can be used. Note that for fast electrons $\nu_\mathrm{d}^\mathrm{ei}$ and $\nu_\mathrm{d}^\mathrm{ee}$ are of the same order, whereas $\nu_\mathrm{s}^\mathrm{ei} \ll \nu_\mathrm{s}^\mathrm{ee}$ and $\nu_\parallel^\mathrm{ei} \ll \nu_\parallel^\mathrm{ee}$ since $v_{T\mathrm{i}} \ll v_{T\mathrm{e}}$. The slowing-down of fast electrons is therefore dominated by collisions with thermal electrons.

If the particles of species a are very fast, relativistic effects have to be included, and particles of the thermal species b can be considered as initially stationary during collisions. Under these circumstances it can be shown that [3]

$$\mathcal{C}_{ab}(f_a, f_b) = \frac{1}{\hat{\tau}_{ab}} \left[\frac{m_a}{m_b p^2} \frac{\partial}{\partial p} \left(\gamma^2 f_a \right) + \frac{\gamma}{p^3} \mathcal{L}(f_a) \right], \tag{2.23}$$

where $p \equiv \gamma v/c$ is the normalised momentum, $\gamma^2 = 1 + p^2$ and

$$\frac{1}{\hat{\tau}_{ab}} = \frac{n_b q_a^2 q_b^2 \ln \Lambda}{4\pi \epsilon_0^2 m_a^2 c^3}. \tag{2.24}$$

2.4 The runaway electron phenomenon

As we have seen, the friction force on an electron with velocity v comes mainly from collisions with other electrons. Eq. (2.17) gives the friction force

$$\frac{m_\mathrm{e} \left\langle \Delta v_\parallel \right\rangle^\mathrm{ee}}{\Delta t} = -m_\mathrm{e} v \nu_\mathrm{s}^\mathrm{ee} \propto G(x_\mathrm{e}). \tag{2.25}$$

The Chandrasekhar function in Fig. 2.2 shows that the friction force exerted on electrons that are faster than the thermal speed, decreases with increasing velocity. The physical reason for this is that a fast electron spends less time in the vicinity of each particle it collides with than a slow electron does. If the electron is very fast, relativistic calculations show that the friction force does not really fall all the way to zero at large energies. It has a minimum at energies around the rest energy, due to the fact that the Coulomb logarithm increases with increasing velocity. The friction force as a function of energy is qualitatively shown in Fig. 2.3.

If there is an electric field in the plasma, electrons above a certain critical velocity v_c experience a friction force smaller than the force from

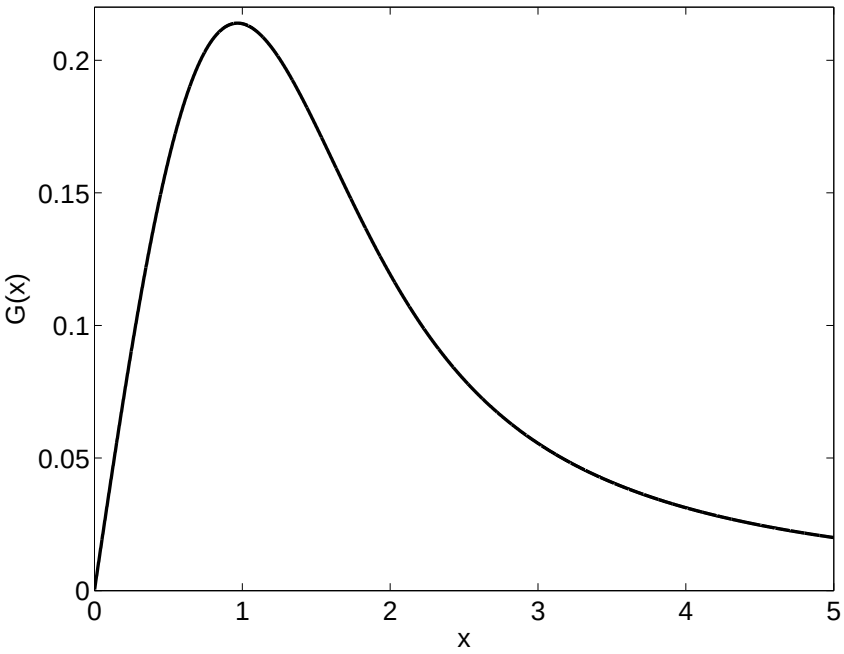

Figure 2.2: The Chandrasekhar function G(x).

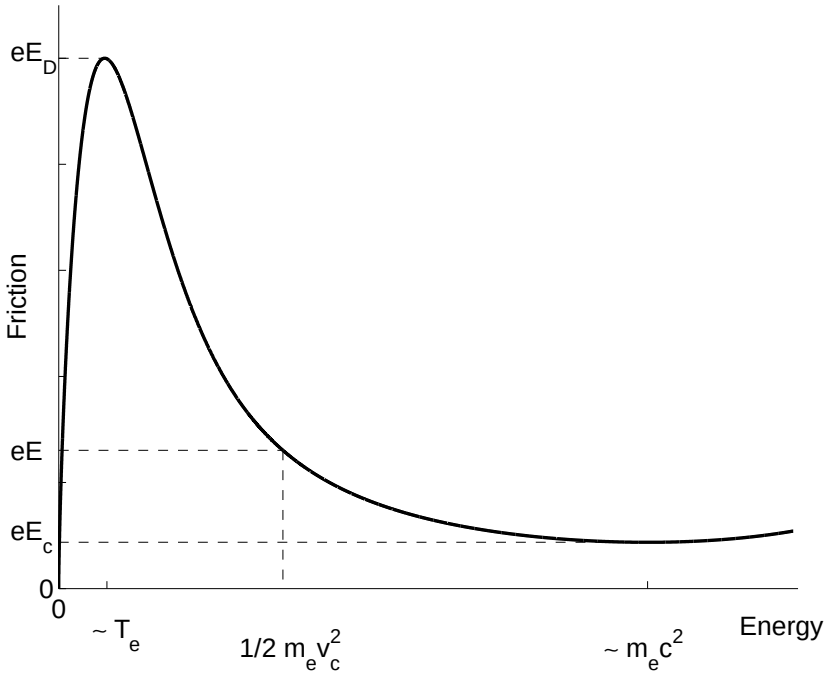

Figure 2.3: Schematic plot of the friction force as a function of the kinetic energy of an electron. If an electric field E is present in the plasma, electrons faster than v_{c} will become runaways.

the electric field. They will be accelerated to very high energies and are called runaway electrons. The threshold energy is found from the force balance $eE = m_\mathrm{e} v \nu_\mathrm{s}^\mathrm{ee}$ to be

$$\frac{m_\mathrm{e} v_\mathrm{c}^2}{2} \equiv \frac{n_\mathrm{e} e^3 \ln\Lambda}{4\pi\epsilon_0^2 E}. \tag{2.26}$$

If the electric field strength becomes as high as the so-called Dreicer field [5, 6]

$$E_\mathrm{D} = \frac{n_\mathrm{e} e^3 \ln\Lambda}{4\pi\epsilon_0^2 T_\mathrm{e}}, \tag{2.27}$$

the whole thermal population will run away because v_c is of the same order as v_T. The smallest electric field needed for runaway generation is found when the critical energy is equal to the rest energy. It is called the critical field E_c [7]:

$$E_\mathrm{c} = \frac{n_\mathrm{e} e^3 \ln\Lambda}{4\pi\epsilon_0^2 m_\mathrm{e} c^2}. \tag{2.28}$$

The electric field needed to drive the current in an ohmic tokamak plasma is usually below E_c. But when a disruption occurs, the induced electric field is often higher than E_c, implying that runaway electrons are indeed generated.

2.5 Runaway electron generation

Runaway electrons can be produced in two essentially different ways, called primary and secondary generation. The classic calculation of primary runaway generation [7–10] assumes that the plasma is in a quasi-steady state. Electrons cross the threshold velocity v_c through diffusion in velocity-space, and are accelerated by the electric field to become runaways. Provided that the runaways are few compared with the whole thermal population, the flux of electrons across the boundary v_c increases the number of runaway electrons at the Dreicer generation rate

$$\frac{dn_\mathrm{run}^\mathrm{I}}{dt} = k n_\mathrm{e} \hat{\nu}_\mathrm{ee} \left(\frac{E_\mathrm{D}}{E_\parallel}\right)^{3(1+Z_\mathrm{eff})/16} \exp\left(-\frac{E_\mathrm{D}}{4E_\parallel} - \sqrt{\frac{(1+Z_\mathrm{eff})E_\mathrm{D}}{E_\parallel}}\right), \tag{2.29}$$

where Z_eff is the effective ion charge and k is a factor of order unity. The corrections to this expression resulting from a relativistic derivation [7,

11] are not included here, since they are small when primary generation is most efficient, i.e. when $E_\parallel \gg E_\mathrm{c}$. In Eq. (2.29) and the remaining part of the thesis, the parallel ($_\parallel$) and perpendicular ($_\perp$) subscripts refer to the direction of the static magnetic field in a tokamak.

In a rapidly cooling plasma the quasi steady-state assumption used in the calculation of the Dreicer generation rate in Eq. (2.29) does not hold. The cooling results in a burst of primary runaways, produced at a rate that can be significantly higher than the Dreicer rate. This "burst" mechanism is studied in detail in Chapter 3 and Papers A and B.

Secondary runaway generation is caused by close Coulomb collisions between existing runaways and thermal electrons. This type of collisions, with impact parameter $b < b_0$, are not included in the previous analysis of this chapter. A runaway electron usually has such a large energy that it can in one close collision knock a thermal electron over the runaway threshold, while still remaining above the threshold itself. This secondary runaway process, described in Ref. [12], leads to a runaway avalanche with the exponential growth rate

$$\frac{1}{n_\mathrm{run}}\frac{dn_\mathrm{run}^\mathrm{II}}{dt} = \frac{E_\parallel/E_\mathrm{c}-1}{\hat{\tau}_\mathrm{ee}\ln\Lambda}\sqrt{\frac{\pi\varphi}{3(Z_\mathrm{eff}+5)}}\times \left(1-\frac{E_\mathrm{c}}{E_\parallel}+\frac{4\pi(Z_\mathrm{eff}+1)^2}{3\varphi(Z_\mathrm{eff}+5)(E_\parallel^2/E_\mathrm{c}^2+4/\varphi^2-1)}\right)^{-1/2} \quad (2.30)$$

where $\varphi = 1 - 1.46\epsilon^{1/2} + 1.72\epsilon$, and $\epsilon = r/R$ is the inverse aspect ratio. The relative importance of primary and secondary generation in tokamak disruptions is studied in Chapter 4.

2.6 Tokamak disruptions

Disruptions are characterised by a sudden temperature drop in the tokamak, caused by heat conduction to the wall and a large influx of impurity (or fuel) particles. The plasma interacts with these particles through excitation and ionisation processes and quickly loses a significant fraction of the stored thermal energy. One way for impurities to enter the plasma is intentionally through gas puffing or pellet injection. Another way is if the plasma reaches a stability limit, and begins to interact strongly with the vessel wall, thereby causing a large influx of wall particles.

During this *thermal quench* phase of the disruption, the temperature falls on a rapid time scale, typically $\lesssim 1$ ms. This leads to a drastically

increasing resistivity η in the plasma, since $\eta \propto T^{-3/2}$. On these short time scales the inductive property of the plasma prevents the current from changing. Hence, when the resistivity rises, Ohm's law $E_\parallel = \eta_\parallel j_\parallel$ implies that an increasing parallel electric field will be induced.

Runaway electrons are produced if $E_\parallel$ becomes higher than the critical field E_c. Once primary runaways are produced by the Dreicer or the burst mechanisms, the secondary avalanche takes over and is usually the dominant generation mechanism. The secondary generation acts on the longest time scale of the runaway processes. This time scale is comparable to the current quench time, the time scale on which the plasma induction (or equivalently resistive diffusion of electric field) allows the current to fall and the radial current density profile to change. The interplay between these processes is studied in Chapter 4 and Paper C.

Disruptions can be harmful for a tokamak in several ways [13]. The heat loads on the vessel and the divertor due to radiation and heat conduction can be tremendous, and if the induced toroidal electric field produces runaway electrons, these may severely damage the first wall upon impact. Vertical displacement events (VDEs) during the plasma current quench is another serious problem. In a VDE, the plasma starts drifting vertically and may transfer a large part of the current to a so-called halo current in the vessel wall. This generates enormous electromagnetic forces on the vacuum vessel and the in-vessel components.

To avoid these serious problems it is desirable to find a controlled way to shut down the plasma before a spontaneous disruption happens. Several methods have been proposed and tested, such as pellet injection [14–16], gas injection [17–20] or even liquid jets [21]. The common aim for these techniques is to avoid halo currents by cooling the plasma enough to make the current decay on a time scale faster than the VDEs. At the same time, runaways should be avoided by a sufficient increase in the electron density. The generation of runaways can also be suppressed by increasing the level of magnetic fluctuations in the plasma [22–24].

2.7 Synchrotron radiation

Unlike the collisional friction force, the reaction force from synchrotron radiation in a magnetised plasma increases when the electron velocity increases. The effect is negligible, however, for all electrons except those travelling at ultra-relativistic velocities. Synchrotron radiation ultimately sets an upper limit to the attainable energy of the runaway

electrons in a tokamak.

Accelerated relativistic charged particles emit radiation in a cone centred around their velocity vector, so the reaction force is anti-parallel to the velocity vector. The synchrotron radiation from charged particles in a tokamak comes both from gyromotion in the static magnetic field and from motion around the torus. For a relativistic electron in the limit of small gyroradius compared to the radius of the torus $\rho \ll R$, the average rate of change of momentum because of synchrotron radiation is [25]

$$\left\langle \frac{dp}{dt} \right\rangle_{\mathrm{rad}} = -\frac{\gamma}{\tau_{\mathrm{r}} p} \left(p_\perp^2 + \frac{\rho_0^2}{R^2} p_\parallel^4 \right), \tag{2.31}$$

$$\left\langle \frac{d\xi}{dt} \right\rangle_{\mathrm{rad}} = -\frac{1}{\gamma^2 p} \left\langle \frac{dp}{dt} \right\rangle_{\mathrm{rad}}, \tag{2.32}$$

where $\xi = p_\parallel / p$, $\tau_{\mathrm{r}} = 6\pi\epsilon_0 (m_{\mathrm{e}} c)^3 / e^4 B^2$ is the radiation time scale, B is the static magnetic field and $\rho_0 = m_{\mathrm{e}} c / eB$.

The reaction force due to synchrotron radiation should be added to the Lorentz force on the left hand side of the Fokker-Planck kinetic equation

$$\frac{\partial f_{\mathrm{e}}}{\partial t} + \frac{\partial}{\partial \mathbf{p}} \cdot \left[\left(\left\langle \frac{d\mathbf{p}}{dt} \right\rangle_{\mathrm{rad}} + \left\langle \frac{d\mathbf{p}}{dt} \right\rangle_{\mathrm{Lorentz}} \right) f_{\mathrm{e}} \right] = \mathcal{C}(f_{\mathrm{e}}), \tag{2.33}$$

where a homogeneous space distribution is assumed. $\mathcal{C}$ is the sum of the collision operator (2.23) for collisions with ions and electrons

$$\mathcal{C}(f_{\mathrm{e}}) = \mathcal{C}_{\mathrm{ee}}(f_{\mathrm{e}}) + \mathcal{C}_{\mathrm{ei}}(f_{\mathrm{e}}) = \frac{1}{\hat{\tau}_{\mathrm{ee}}} \left[\frac{1}{p^2} \frac{\partial}{\partial p} \left(\gamma^2 f_{\mathrm{e}} \right) + (1+Z) \frac{\gamma}{p^3} \mathcal{L}(f_{\mathrm{e}}) \right], \tag{2.34}$$

where Z is the ion charge. As in the non-relativistic case, collisions with ions cause only pitch-angle scattering. Using the cosine of the pitch-angle $\xi \equiv p_\parallel / p = \cos\theta$, the Lorentz operator Eq. (2.15) can be written as

$$\mathcal{L} = \frac{1}{2} \frac{\partial}{\partial \xi} (1 - \xi^2) \frac{\partial}{\partial \xi}. \tag{2.35}$$

When an electric field $E_\parallel > E_{\mathrm{c}}$ is present in the plasma, a strongly relativistic runaway electron beam with $p \gg 1$ and $1 - \xi \ll 1$ can easily form. In this high energy tail of the distribution $p_\perp \ll p_\parallel$, and it is suitable to change coordinates from (p, ξ) to $(p_\parallel, p_\perp)$. Let $E = E_\parallel / E_{\mathrm{c}}$

and note that $\gamma \simeq p \simeq p_\parallel$. The kinetic equation then takes the form

$$\frac{\partial f}{\partial t} + \frac{E-1}{\hat{\tau}_{\rm ee}}\frac{\partial f}{\partial p_\parallel} - \frac{1}{\tau_{\rm r}}\frac{\partial}{\partial p_\parallel}\left[\left(p_\perp^2 + \frac{\rho_0^2}{R^2}p_\parallel^4\right) f\right] = \frac{1+Z}{2\hat{\tau}_{\rm ee}p_\perp}\frac{\partial}{\partial p_\perp}\left(p_\perp \frac{\partial f}{\partial p_\perp}\right), \tag{2.36}$$

where the index e on the distribution function has been dropped. The slowing-down term has been incorporated in the second term on the left hand side of the equation leaving only pitch-angle scattering on the right. Equation (2.36) is studied further in Sec. 5.3 and in Paper D.

2.8 Momentum space dynamics

If pitch-angle scattering is neglected the electrons will follow well-defined orbits in momentum space. An example of the resulting map of momentum space is shown in Fig. 2.4, where $\hat{\tau}_{\rm ee}/\tau_{\rm r} = 0.1$ (which is valid for $B = 3$ T, $n_{\rm e} = 3 \cdot 10^{19}$ m^{-3}) and $E = 1.2$. There is a distinct separatrix (the dashed line) between the runaway region and the thermal region, given by the orbit through the point $p_\perp = 0$, $p_\parallel = p_{\rm c}$, where $p_{\rm c}$ is the critical momentum. Thermal electrons that undergo collisions with strongly relativistic runaways travelling in the parallel direction perform a jump in momentum space to a place on the dotted line $\xi = p/(\sqrt{1+p^2}+1)$ [12]. Those electrons that land inside the runaway region will contribute to the secondary runaway rate. At the same time pitch-angle scattering will cause electrons to cross the separatrix from the runaway region to the thermal region. If E is lowered, the separatrix will move towards higher $p_\parallel$, and ultimately the runaway region disappears completely when $E = 1$. This means that it is possible to consider a steady-state situation ($\partial f/\partial t = 0$) in a tokamak plasma with $E = E_{\rm t} > 1$. The threshold electric field $E_{\rm t}$ is given by the value which produces a balance between the secondary runaway rate and pitch-angle scattering across the separatrix.

In the high energy tail of the runaway distribution, the electric field must, in a steady-state situation, be balanced by radiation reaction and pitch-angle scattering, according to Eq. (2.36). This situation has been investigated in Paper D, where the problem of determining the functional form of the distribution function in the tail has been addressed. The fact that the electrons in the high energy part of the runaway region decelerate or accelerate depending on $p_\perp$ makes this problem mathematically interesting. The dash-dotted line in Fig.2.4 shows $p_\perp = p_{\perp\text{two-way}} = \sqrt{(E-1)\tau_{\rm r}/\hat{\tau}_{\rm ee}}$. Particles with $p_\perp > p_{\perp\text{two-way}}$ move

towards lower $p_\parallel$ (decelerate) and particles with $p_\perp < p_{\perp\text{two-way}}$ move towards higher $p_\parallel$ (accelerate). When pitch-angle scattering is added it is seen that this problem is of a two-way diffusion type. This class of problems has been investigated mathematically in both Papers D and E, and the theory will be presented in the Chapter 5.

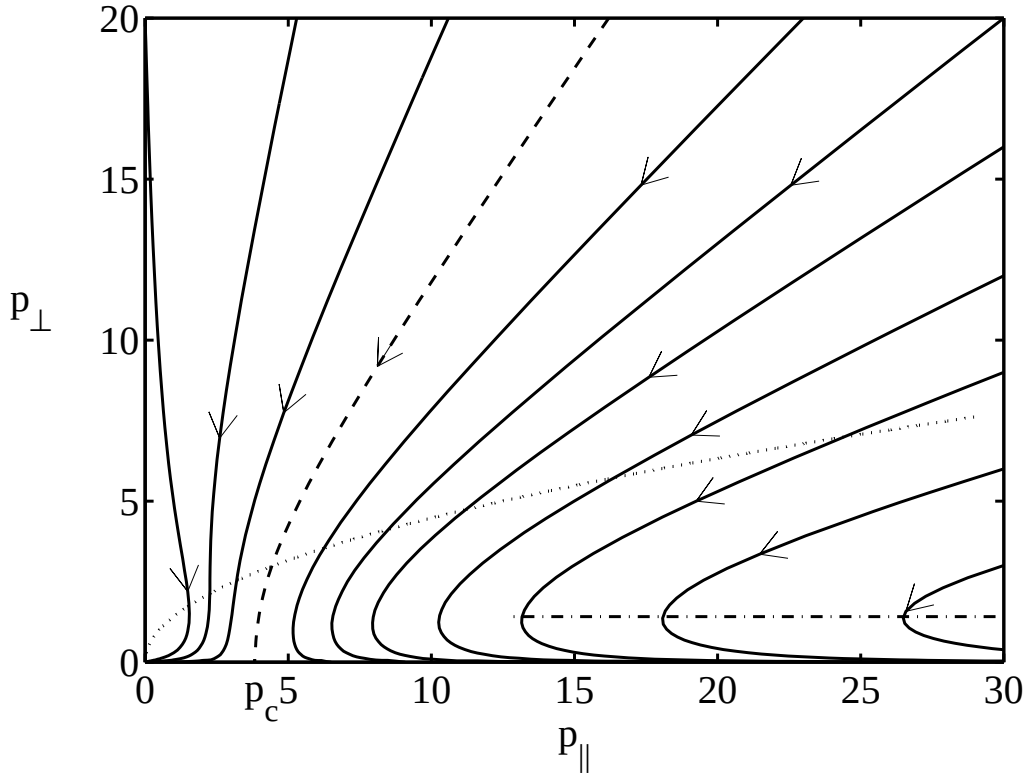

Figure 2.4: Particle traces in momentum space for $E_\parallel/E_\text{c} = 1.2$ and $\hat{\tau}_\text{ee}/\tau_\text{r} = 0.1$. The runaway region is to the right of the dashed line, which shows the orbit ending in the stagnation point at $p_\perp = 0$, $p_\parallel = p_\text{c}$. The dotted line shows where the avalanche runaway electrons are born and the dash-dotted line separates the regions where $\dot{p}_\parallel < 0$ and $\dot{p}_\parallel > 0$ in the runaway tail.

Chapter 3

Runaway generation in a cooling plasma

In tokamak disruptions a large number of runaway electrons can be produced. This chapter addresses the question of how large the *primary* runaway population may become. The generation of primary runaways in tokamak disruptions is considered in the first Section. In Section 3.2 the theory developed in Paper A concerning the kinetics of a cooling plasma is described, and the resulting higher level of runaway production as compared to ordinary Dreicer generation is studied Section 3.3 (Paper B).

3.1 The runaway burst mechanism

In the thermal quench of a disruption, it is mostly the thermal electrons that lose energy because of interaction with the entering impurities. The superthermal electrons are slowed down primarily by collisions with the thermal electrons. The fact that the collision frequency decreases with increasing energy, has the effect that fast electrons lose energy less quickly than slower ones and a high-energy tail therefore develops as the plasma cools down. A part of this tail, consisting of electrons that have not had time to thermalise, can be converted into a "burst" of runaways.

If the plasma cools down on a time scale t_0 shorter than the collision time for electrons near the runaway threshold, it is not appropriate to assume that the electron distribution function is stationary below the critical velocity v_c, as the ordinary calculation of the Dreicer generation Eq. (2.29) does. The evolution of the tail of the velocity distribution

has to be calculated more accurately from the kinetic equation. Such a calculation is performed in Paper A, under the assumption that the influence of the electric field on the distribution function is negligible compared with the effect of the cooling. This greatly simplifies the calculations, since the electron velocity distribution function remains isotropic. In Paper B the resulting runaway production is estimated by counting the number of electrons of this isotropic distribution inside the (non-isotropic) runaway region of velocity space set up by the electric field.

3.2 Electron kinetics in a cooling plasma: Paper A

The pitch-angle averaged kinetic equation for fast electrons in a homogeneous plasma can be obtained from Eqs. (2.3) and (2.14). When the effects of frictional slowing down and energy diffusion are included, it becomes

$$\frac{\partial f}{\partial t} = \frac{1}{2v^2}\frac{\partial}{\partial v}v^3\left(\nu_{\mathrm{s}}^{\mathrm{ee}} f + \nu_{\parallel}^{\mathrm{ee}}\frac{\partial f}{\partial v}\right) + \frac{1}{v^2}\frac{\partial}{\partial v}\left(\nu^{\mathrm{e}z} v^3 f\right), \tag{3.1}$$

where the $\nu^{\mathrm{e}z}$ term describes energy loss due to inelastic collisions involving ionisation and excitation of impurities. This term is only important for the thermal part of the distribution and does not affect the high-energy tail, since it decays at high energies as $\nu^{\mathrm{e}z}(v) \sim v^{-3}$. The collision frequencies $\nu_{\mathrm{s}}^{\mathrm{ee}}$ and $\nu_{\parallel}^{\mathrm{ee}}$ where defined in terms of $\hat{\nu}_{\mathrm{ee}}$ in Eqs. (2.17)–(2.19).

It is convenient to normalise time to $\hat{\nu}_{\mathrm{ee}}^{-1}$ by writing $ds = \hat{\nu}_{\mathrm{ee}}dt$, the velocity to $v_T(t) = [2T(t)/m_{\mathrm{e}}]^{1/2}$ by writing $x = v/v_T$, and the distribution function by writing $F = f v_T^3 \pi^{3/2}/n$. The electron density n is assumed to be constant in time, but v_T varies because of the cooling. Consequently, the time derivative in Eq. (3.1) together with the velocity and distribution function normalisations introduce two new terms in the kinetic equation, which becomes

$$\frac{\partial F}{\partial s} + \delta\left(3F + x\frac{\partial F}{\partial x}\right) = \frac{1}{x^2}\frac{\partial}{\partial x}\left(F + \frac{1}{2x}\frac{\partial F}{\partial x}\right), \tag{3.2}$$

where

$$\delta = -\frac{1}{2\hat{\nu}_{\mathrm{ee}}}\frac{d\ln T}{dt}, \tag{3.3}$$

and T is the electron temperature. The initial condition is for simplicity taken to be a Maxwellian distribution $F(x,0) = e^{-x^2}$.

Equation (3.2) becomes analytically tractable if one assumes that the parameter δ is independent of time. This requires that the temperature changes in time according to

$$T(t) = T_0(1 - t/t_0)^{2/3}, \tag{3.4}$$

where the cooling time t_0 can be written in terms of δ and the initial collision frequency as $t_0 = 1/(3\hat{\nu}_{\mathrm{ee}}(0)\delta)$. This temperature evolution is a good model at least for the early stages of the thermal quench in a tokamak disruption.

If the plasma is assumed to cool down slowly relative to the thermal collision time, δ is small and an expansion procedure can be performed. The analysis involves matching expansions in five regions of velocity space. As $t \to t_0$, $s \to \infty$ and the temperature (3.4) goes to zero, the distribution function asymptotically approaches the solution

$$\begin{aligned}
&\lim_{t\to t_0} f(y,t) = n\left(\frac{m}{2\pi T}\right)^{3/2} \times \\
&\times \begin{cases}
\exp\left[-\frac{1}{\delta^{2/3}}\left(y^2 - \frac{2y^5}{5}\right)\right], & y < 1 \\
\frac{1}{2}\exp\left[\frac{3}{\delta^{2/3}}\left((y-1)^2 - \frac{1}{5}\right)\right]\operatorname{erfc}\left(\frac{\sqrt{3}(y-1)}{\delta^{1/3}}\right), & y - 1 \sim \delta^{1/3} \\
\frac{\delta^{1/3}}{2}\left(\frac{3}{\pi}\right)^{1/2}\exp\left(-\frac{3}{5\delta^{2/3}}\right)\frac{1}{y^3-1}, & y > 1
\end{cases}
\end{aligned} \tag{3.5}$$

where $y = x\delta^{1/3}$. The tail of the distribution function grows in time and approaches the asymptotic solution approximately at the time $s \sim \delta^{-1}\ln y$.

The asymptotic solution agrees well with direct numerical solutions of Eq. (3.2). An example is shown in Fig. 3.1. The numerical solution was found by a finite difference discretisation of Eq. (3.2) and was checked by comparing with a similar simulation using the ARENA Monte Carlo code [26].

The distribution function given by Eq. (3.5) is self-similar in the sense that although its height increases and its width shrinks as the plasma cools down, its shape does not change with time when the distribution function is expressed in the re-scaled velocity variables.

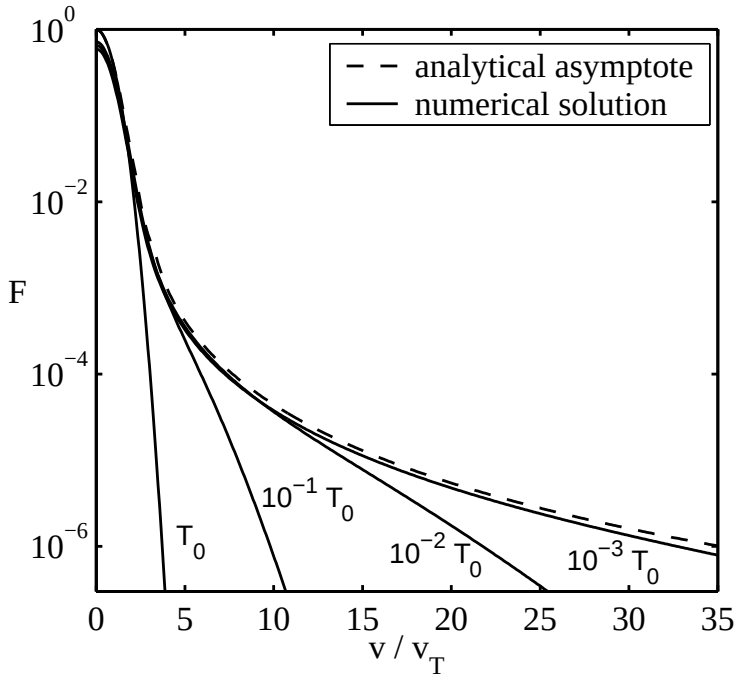

Figure 3.1: Comparison of a direct numerical solution of Eq. (3.2) and the asymptotic end-state given by (3.5) for $\delta = 0.05$. The numerical solutions are given at the times when the temperature has fallen to $T = T_0$, $10^{-1}T_0$, $10^{-2}T_0$, and $10^{-3}T_0$.

3.3 Runaways in a cooling plasma: Paper B

The number of runaways generated by the burst mechanism is determined by the tail electrons, whose number is likely to be enhanced for plasmas typical of present and future experiments. This may be especially important for disruptions in ITER, where the projected electron temperature is around 20 keV and the collision time is therefore not very much shorter than the characteristic time of the thermal quench of a disruption. Clearly, the electron temperature does not necessarily follow Eq. (3.4) during a tokamak disruption where the impurity content changes rapidly with time, but the qualitative behaviour of the tail formation should be similar.

The theory from Paper A is used in Paper B to obtain an approximation for the number of runaways in a disruption by integrating the distribution function over the runaway region in velocity space (the region to the right of the dashed line in Fig. 2.4). The runaway region is determined by the instantaneous temperature and the induced parallel electric field. Since the electric field was excluded in the previous

section, it is necessary to neglect the effect that the electric field breaks the isotropy in velocity space and pulls out a tail in the distribution function in the parallel direction. Nevertheless, this has a surprisingly small effect on the number of tail particles in a cooling plasma, as has been shown by full numerical simulations in Paper B.

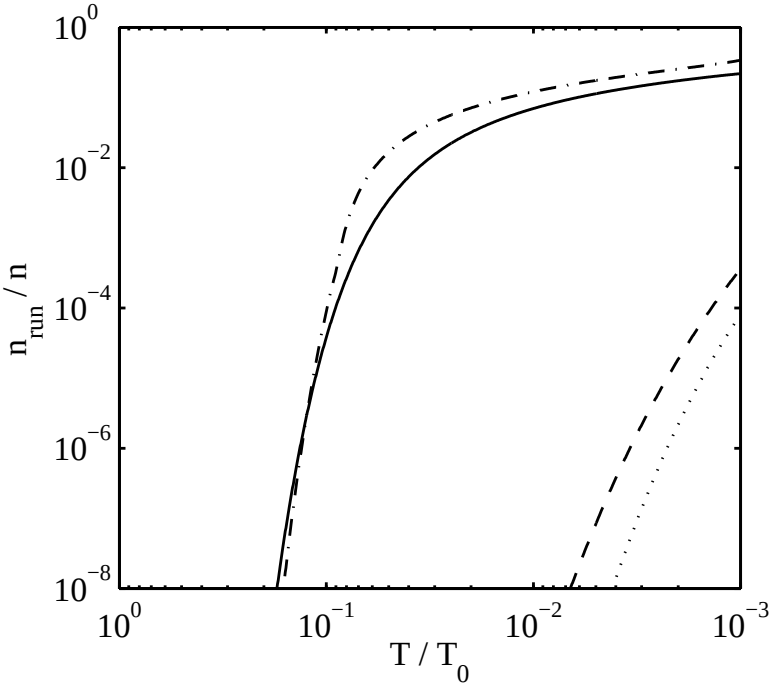

Figure 3.2: The number of runaways from numerical solution of Eq. (3.2) (solid) and from analytical integration of Eq. (3.5) (dash-dotted) are plotted against the reached fraction T/T_0 of the original temperature. The Dreicer production (dashed) and the number of electrons in the runaway region of a Maxwellian (dotted) are also shown. The parameters used are $E_{\mathrm{D}0}/E_0 = 530$ and $\delta = 0.05$.

The number of electrons in the runaway region has been calculated both by integrating Eq. (3.5) analytically over the runaway region, and using the numerical scheme mentioned in the previous section. The results of both these methods are presented in Fig. 3.2 for a typical JET case together with the usual Dreicer production, and it is found that the burst mechanism is much more efficient than the Dreicer generation. The reason is that as long as the critical velocity lies in the outer region of Eq. (3.5) (where $y > 1$) the distribution function over the runaway threshold is much larger than a Maxwellian. The inequality

$y_c = \delta^{1/3} v_c / v_T > 1$ corresponds to the criterion

$$\nu_0 t_0 < \frac{1}{3} \left(\frac{E_D}{2E_\parallel} \right)^{3/2}, \tag{3.6}$$

where $\nu_0 = \hat{\nu}_{ee}(0)$ is the initial collision frequency and $E_D/E_\parallel$ should be calculated at the final temperature. Eq. (3.6) gives a limit on how fast the plasma has to cool down for the burst to be more important than Dreicer production.

The numerical scheme can be used to predict the runaway production for other types of temperature evolution than the one in Eq. (3.4). Such simulations show that the size of the runaway burst depends sensitively on the particular type of evolution. An exponential temperature decay, for instance, gives less runaways than the evolution in Eq. (3.4) if comparable time scales and the same final temperature are used. Nevertheless, the burst mechanism dominates over Dreicer generation in both cases.

The density of electrons usually rises during a disruption due to ionisation of impurity atoms. The resulting increase of collisionality causes a decrease in the runaway production. This is especially important in experiments where so-called killer pellets are injected to cool the plasma. Numerical simulations in connection with such experiments [16,27] show that a burst of runaway production occurs as the temperature falls.

The increasing density has three important effects that can decrease the burst generation of runaways. Firstly, the critical electric field E_c increases. Secondly, the runaway region moves towards higher velocities because of the density dependence of E_D. The third effect is a reduction of the high-energy tail caused by the rapid cooling. In Paper B the theory involving asymptotic matching of the distribution function is extended to include also a varying density, and the distribution function is calculated for the special case when $\lambda = 1/(n\hat{\nu}_{ee}) dn/dt$ and δ are constant in time. This corresponds to the density and temperature evolution

$$n(t) = n_0 (1 - t/t_0)^{-\lambda/(3\alpha\delta)}, \tag{3.7}$$

$$T(t) = T_0 (1 - t/t_0)^{2/(3\alpha)}, \tag{3.8}$$

where $\alpha = 1 + \lambda/(3\delta)$. The asymptotic distribution function becomes

$$\lim_{t \to t_0} F(y,t) =$$

$$= \begin{cases} (1-y^3)^{\alpha-1} \exp\left[-\delta^{-2/3}\left(y^2 - \frac{2y^5}{5}\right)\right], & y < 1 \\ \left(\sqrt{3}\delta^{1/3}\right)^{\alpha-1} 2^{-\alpha/2} \frac{\Gamma(\alpha)}{\sqrt{\pi}} \exp\left[\left(\frac{3}{2}(y-1)^2 - \frac{3}{5}\right)\delta^{-2/3}\right] \times \\ \qquad \times D_{-\alpha}\left[\sqrt{6}(y-1)\delta^{-1/3}\right], & y - 1 \sim \delta^{1/3} \\ \left(\sqrt{3}\delta^{1/3}\right)^{2\alpha-1} 2^{-\alpha} \frac{\Gamma(\alpha)}{\sqrt{\pi}} \exp\left[-\frac{3}{5}\delta^{-2/3}\right] \frac{1}{(y^3-1)^\alpha}, & y > 1 \end{cases} \tag{3.9}$$

where $D_{-\alpha}$ is a parabolic cylinder function [28]. Eq. (3.9) reduces to Eq. (3.5) when $\lambda = 0$, because $D_{-1}(r\sqrt{6}) = \sqrt{\pi/2}\exp(3r^2/2)\mathrm{erfc}(r\sqrt{3})$. Analytic integration of Eq. (3.9) agrees well with numerical simulations of the corresponding kinetic equation, see Fig. 3.3. The result is a smaller runaway burst than in the constant density case in Fig. 3.2, but it is now much larger than Dreicer generation, which is almost completely suppressed by the increased critical velocity.

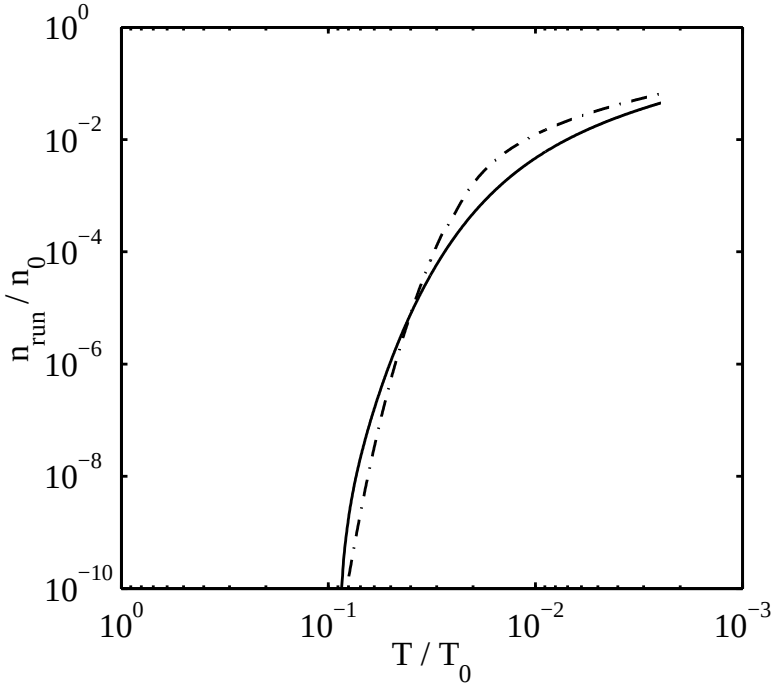

Figure 3.3: The analytical (dash-dotted) and numerical (solid) estimates of the runaway density when the temperature has fallen to a fraction T/T_0 of its original value. Here $E_{\mathrm{D}0}/E_0 = 530$ and $\lambda = \delta = 0.05$.

Chapter 4

Current dynamics during tokamak disruptions

In tokamak disruptions, runaway generation affects the evolution of the current density profile. A model for this process is presented here, and the results of Paper C are discussed.

4.1 Current and runaway dynamics

In a disruption, the evolution of the current and the runaway production are closely connected through the toroidal electric field $E_\phi \simeq E_\parallel$. This electric field is induced during the thermal quench due to the increasing resistivity, and it may cause primary and secondary runaway electrons to be produced. The current carried by the runaway electrons replaces a part of the Ohmic current, thereby limiting the further growth of the electric field. At the same time, the electric field diffuses out through the resistive plasma on a time scale much longer than the thermal quench, and it continues to produce runaways as long as $E_\parallel > E_\mathrm{c}$. Towards the end of the disruption virtually all current is carried by runaways, since the remaining electric field is too weak to drive any significant Ohmic current.

These processes have been studied previously [29–32] using a zero-dimensional model, where the on-axis electric field E_axis and the current I are related through the induction equation

$$E_\mathrm{axis} = -\frac{L}{2\pi R}\frac{dI}{dt}, \tag{4.1}$$

and the inductance is $L \sim R\mu_0$. In Ref. [29] a simple criterion was derived for whether or not a substantial fraction of the initial current becomes converted to runaway current in the disruption. This theory is refined in the Appendix of Paper C and the result is that substantial runaway production occurs if a certain parameter H is positive, where

$$H \equiv \frac{\sqrt{2\pi}}{3}\frac{I_0}{I_{\rm A}\ln\Lambda} - \frac{E_{\rm D}}{4E_\parallel} - \sqrt{\frac{2E_{\rm D}}{E_\parallel}} + \ln\frac{m_{\rm e}c^2}{T_{\rm e}} + \frac{11}{8}\ln\frac{E_{\rm D}}{E_\parallel}, \qquad (4.2)$$

and $I_{\rm A} = 4\pi m_{\rm e}c/(\mu_0 e)$ is the Alfvén current. In this expression, the quantities $E_{\rm D}$, $E_\parallel$ and $T_{\rm e}$ should be evaluated just after the thermal quench.

4.2 Radial profiles of current and runaway density: Paper C

One-dimensional models, which take into account the evolution of the radial profiles of the electric field and the runaway density, were proposed in Refs. [33, 34]. The model in Ref. [34] is studied in more detail in Paper C. It consists of two coupled equations describing the evolution of the electric field and the runaway electron density. The runaway rate is given by

$$\frac{\partial n_{\rm run}}{\partial t} = \frac{\partial n_{\rm run}^{\rm I}}{\partial t} + \frac{\partial n_{\rm run}^{\rm II}}{\partial t}, \qquad (4.3)$$

where the primary and secondary runaway generation rates $\partial n_{\rm run}^{\rm I}/\partial t$ and $\partial n_{\rm run}^{\rm II}/\partial t$ are found from Eqs. (2.29) and (2.30). This is coupled to the parallel component of the local induction equation in a cylindrical approximation,

$$\frac{1}{r}\frac{\partial}{\partial r}\left(r\frac{\partial E_\parallel}{\partial r}\right) = \mu_0\frac{\partial j_\parallel}{\partial t}, \qquad (4.4)$$

which is a refinement of Eq. (4.1). For simplicity, the burst generation mechanism is omitted in Eq. (4.3), because it would extend the problem to include also the velocity dynamics of the electrons. Radial diffusion of runaways due to magnetic field fluctuations [24] is also neglected.

The current density $j_\parallel$ consists of both Ohmic current and runaway current. If one neglects the time required to accelerate a newly generated runaway electron to relativistic speeds, the runaway current can be calculated by assuming that all runaways travel at the speed of light.

The total current density becomes $j_\parallel = \sigma_\parallel E_\parallel + n_{\rm run} ec$, where $\sigma_\parallel$ is the Spitzer conductivity ($\propto T_{\rm e}^{3/2}$) augmented with a neoclassical correction.

Equations (4.3) and (4.4) can be written in a normalised form as

$$\frac{\partial n}{\partial t'} = F(E, t', x) + nE, \tag{4.5}$$

$$\frac{1}{\alpha x}\frac{\partial}{\partial x} x \frac{\partial E}{\partial x} = \frac{\partial}{\partial t'}(\sigma E + n), \tag{4.6}$$

where $t' = t/(3\sqrt{2/\pi}\hat{\tau}_{\rm ee} \ln\Lambda)$, $x = r/a$, and a is the plasma minor radius. Furthermore, $n = n_{\rm run} ec/j_{\parallel 0}$ is the runaway current density normalised to the initial on-axis current density, $E = E_\parallel/E_{\rm c0}$ is the electric field normalised to the initial critical field on axis, $\sigma = \sigma_\parallel E_{\rm c0}/j_{\parallel 0}$, and $\alpha = (2\pi)^{3/2} j_{\parallel 0} a^2/(3 \ln\Lambda I_{\rm A})$. The function $F(E, t', x)$ describes primary generation, and the avalanche is produced by the second term on the right hand side of Eq. (4.5).

To understand the processes included in the model, it is useful to compare the different time scales of the problem. For realistic disruptions the fastest time scale is the thermal quench time (~ 0.5 ms). After the temperature drop a runaway seed is formed by primary generation. This seed is amplified by the secondary avalanche on a time scale comparable to the time scale of electric field diffusion. Given the seed profile, the competition between secondary generation and field diffusion determines the final runaway current. Of crucial importance is the parameter α, which is proportional to the initial current. If the seed is small or the initial current low, secondary generation takes a long time to build up and only a small part of the initial current is converted into runaway current. If, on the other hand, the seed is large or the initial current is high, the secondary mechanism can be fast and the current conversion ratio high.

The dynamics of the coupled system of equations. (4.5) and (4.6) is investigated both numerically and analytically in Paper C. In the numerical simulations, the temperature is assumed to decay exponentially according to

$$T_{\rm e}(r) = T_{\rm final}(r) + [T_0(r) - T_{\rm final}(r)] e^{-t/t_0}. \tag{4.7}$$

The results from a simulation of a typical JET disruption (discharge no. 63133) with $T_0(0) = 3.1$ keV and $t_0 = 0.5$ ms agrees roughly with the experiment if the post-disruption temperature $T_{\rm final}$ is chosen to be around 10 eV. The post-disruption runaway current is around 2/3 of the

initial current and the current falls on a time scale of roughly 5 ms as shown in Fig. 4.1.

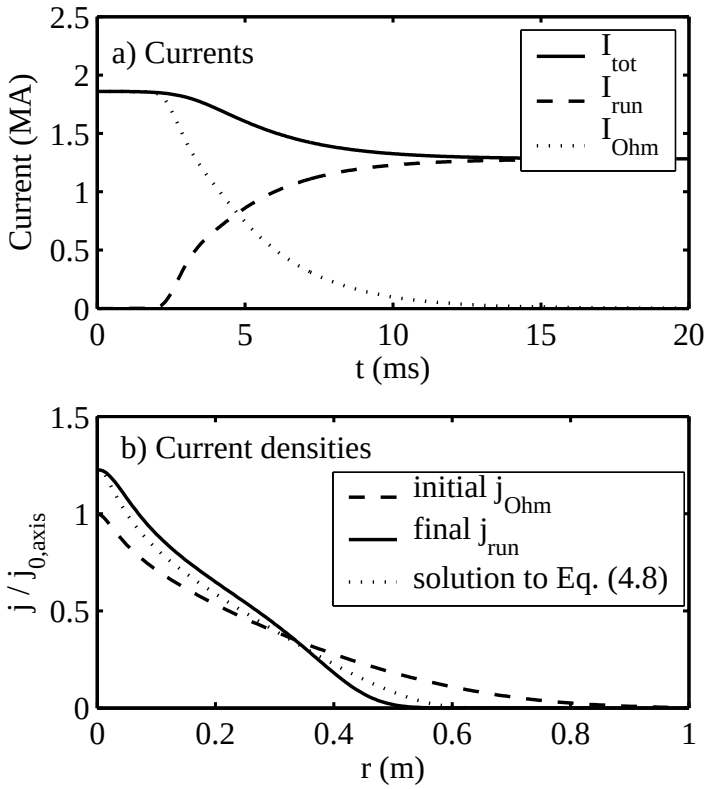

Figure 4.1: A disruption simulation using temperature and density profiles from JET discharge 63133 and $t_0 = 0.5$ ms. (a) The evolution of the current. (b) The radial profiles of the current density before and after the disruption.

Primary runaway generation is often most efficient in the central plasma, because neoclassical effects and flattening of the temperature profile during the thermal quench both make the relative change in conductivity become largest on the magnetic axis, generating a high central electric field. This leads to the interesting phenomenon, shown in Fig. 4.1b, that the post-disruption current density profile is more peaked on the magnetic axis than the initial Ohmic current. The on-axis current density does in fact increase during the disruption, although the total current falls. This happens because the efficient runaway generation in the centre of the plasma produces a runaway current there, which replaces a large part of the Ohmic current and limits the growth of the central electric field. Some time after the thermal quench the electric field will have an off axis maximum and start to diffuse inwards, which

further strengthens the runaway production in the plasma centre and causes the peaking of the current profile.

To explore the different possible evolution scenarios for a disrupting plasma, a parameter scan was performed around the reference JET discharge. Varying the electron density n_e, the final temperature T_final and the initial current I_0 revealed three qualitatively different regions of parameter space: one with very low runaway production ($n_\mathrm{e} \gtrsim 10^{20}$ m^{-3}, $T_\mathrm{final} \gtrsim 200$ eV, $I_0 \lesssim 0.5$ MA), a second, middle region with high on-axis runaway current peaking and predominantly secondary generation, and a third where primary generation is effective enough to reproduce the initial current profile ($n_\mathrm{e} \lesssim 10^{19}$ m^{-3}, $T_\mathrm{final} \lesssim 10$ eV, $I_0 \gtrsim 5$ MA). The transition between the first and second regions appears approximately where the parameter H, defined in Eq. (4.2), is zero.

The analytical investigation in Paper C is based on the time scale arguments mentioned above. Since the thermal quench usually has the shortest time scale, it can be taken to be infinitely fast. What happens next can be divided into two stages. In the first stage the runaway seed density $n_\star(x)$ is determined assuming that electric field diffusion can be neglected on this short time scale. In the second stage primary generation is instead negligible, and field diffusion and secondary generation together determine the final current profile. The second stage is governed by the equation

$$\frac{1}{\alpha x}\frac{\partial}{\partial x} x \frac{\partial}{\partial x}(N - N_\star) + j_\star - e^N = 0, \tag{4.8}$$

where $N = \ln n$ is the final runaway profile, $N_\star = \ln n_\star$ is the seed, and $j_\star$ is approximately equal to the initial current profile. Since the highest derivative operates on $N - N_\star$, this difference is not allowed to have sudden jumps in its radial dependence. Any small scale radial ripple in the seed $n_\star(x)$ therefore becomes amplified in the final current profile $n(x)$. This has also been seen in numerical simulations, where an assumed small radial perturbation in the thermal quench time t_0 causes the runaway current to become radially filamented. Furthermore, the on-axis current peaking phenomenon discussed above is also described by Eq. (4.8). Figure 4.1b shows that one obtains a good approximation for the final runaway current profile by solving Eq. (4.8). The peaking of the final current profile may have implications for the stability of the post-disruption plasma.

Chapter 5

Two-way diffusion equations

This chapter describes a general approximation scheme for solving two-way diffusion equations, considered in Paper D, and demonstrates how it can be used for solving two electron beam problems. The first problem, considered in Papers D and E, is the effect of back-scattering on one-dimensional electron beam transport. The second example, also analysed in Paper D, is the problem of determining the steady-state runaway electron beam distribution function at high energies, where synchrotron radiation and pitch-angle scattering balance the electric field in the Fokker-Planck equation.

5.1 A general solution scheme

The general two-way diffusion equation in one dimension is [35]

$$h(\mu)\frac{\partial f(z,\mu)}{\partial z} = \frac{\partial}{\partial \mu} D(\mu)\frac{\partial f(z,\mu)}{\partial \mu} \equiv \mathcal{L}(f) \tag{5.1}$$

The equation is to be solved in the domain $0 < z < L$, $a < \mu < b$, and the diffusion coefficient $D(\mu)$ is assumed to be positive. The coefficient $h(\mu)$, however, changes sign at least once in the interval $a < \mu < b$, which gives rise to the two-way diffusion character of the equation. Diffusive spreading in μ is directed towards increasing z on the parts of the interval where h is positive, and towards decreasing z where h is negative. If z is thought of as time, this means that time has reverse direction in the regions where $h < 0$.

Apart from at $\mu = a$ and $\mu = b$, boundary conditions also have to be specified at $z = 0$ where $h > 0$, and at $z = L$ where $h < 0$

$$\begin{aligned} f(0, \mu) &= f_+(\mu), \quad h(\mu) > 0, \\ f(L, \mu) &= f_-(\mu), \quad h(\mu) < 0. \end{aligned} \tag{5.2}$$

It is instructive to think of these as "initial" conditions, since "time" is directed from these boundaries into the domain. If z instead denotes a space coordinate, the boundary conditions Eq. (5.2) correspond to specifying the distribution of the particles that enter the medium, while the equation itself determines the distribution of emitted particles.

Separation of variables transforms Eq. (5.1) into the eigenvalue problem

$$\mathcal{L}(f_n) = -\lambda_n h(\mu) f_n(\mu), \tag{5.3}$$

where the eigenvalues λ_n are sorted in rising order and the integer indices n have the same sign as the corresponding λ_n. The eigenfunctions

$$f(z, \mu) = f_n(\mu) e^{-\lambda_n z} \tag{5.4}$$

are solutions to Eq (5.1) if the boundary conditions are ignored. Since h changes sign in the interval $a < \mu < b$, the conventional Sturm-Liouville theory does not apply and these eigenfunctions do not necessarily form a complete and orthogonal system. However, if a solution $g(\mu)$ exists to the equation

$$\frac{\partial}{\partial \mu} D(\mu) \frac{\partial g(\mu)}{\partial \mu} + h(\mu) = 0, \tag{5.5}$$

the system of eigenfunctions (5.4) is made complete if it is supplemented by the additional non-separable solution $f_D(z, \mu) = z - g(\mu)$ (the so-called diffusion solution) to Eq. (5.1).

The eigenfunctions $f_n(\mu)$ with positive eigenvalues together with $g(\mu)$ form a complete set on the interval where $h(\mu) > 0$ [35, 36]. Consequently, the boundary data at $z = 0$ can be expanded as

$$f_+(\mu) = \alpha g(\mu) + \sum_{n \geq 0}^{\infty} c_n f_n(\mu). \tag{5.6}$$

However, the eigenfunctions are not orthogonal and the expansion coefficients are therefore not easily calculated. Similarly, the data on the other boundary $f_-(\mu)$ can be expanded in the eigenfunctions with negative

eigenvalues, which form a complete set on the interval where $h(\mu) < 0$. The general solution to Eq (5.1) can thus be expanded as follows

$$f(z,\mu) = c_0 f_0(\mu) + \alpha f_D(z,\mu) + \\ + \sum_{n>0} \left(c_n f_n(\mu) e^{-\lambda_n z} + c_{-n} f_{-n}(\mu) e^{-\lambda_{-n}(z-L)} \right). \quad (5.7)$$

These results suggest that approximate solutions to the two-way diffusion problem can be constructed in a systematic way. If L is not too small, one expects that the solution $f(z,\mu)$ can be represented with reasonable accuracy by the first few eigensolutions in most of the domain. The higher-order eigenfunctions have large eigenvalues and are strongly suppressed inside the region. These terms should contribute to the solution only in narrow boundary layers close to the boundaries.

The simplest approximation of $f(z,\mu)$ was determined in a classic paper by Bethe *et al.* [37], and consists in neglecting all the exponentially damped terms in Eq (5.7),

$$f(z,\mu) \simeq c_0 f_0(\mu) + \alpha f_D(z,\mu) = c_0 + \alpha(z - g(\mu)). \quad (5.8)$$

The problem investigated in [37] is that of scattering of mono-energetic electrons, and it will be discussed in detail in the next section. In this problem, $h(\mu) = g(\mu) = \mu$, $D(\mu) = (1-\mu^2)/2$, $a = -1$, $b = 1$, and the coefficients c_0 and α were determined by the physical constraint that the approximate solution should describe the correct flux of electrons entering the scattering medium,

$$\int_{h(\mu)>0} f(0,\mu)\mu d\mu = \int_{h(\mu)>0} f_+(\mu)\mu d\mu, \quad (5.9)$$

$$\int_{h(\mu)<0} f(L,\mu)\mu d\mu = \int_{h(\mu)<0} f_-(\mu)\mu d\mu. \quad (5.10)$$

In the case of a collimated electron beam with perpendicular incidence, the boundary conditions become $f_+(\mu) = \delta(\mu - 1)$ and $f_-(\mu) = 0$ and one obtains $\alpha = -6/(4+3L)$ and $c_0 = 2(1+\alpha/3)$. The total transmitted flux is then given by [37]

$$\Gamma = \int_{-1}^{1} f(z,\mu)\mu d\mu = -\alpha\frac{2}{3} = \frac{1}{1+3L/4}. \quad (5.11)$$

By generalising the procedure of Bethe *et al.*, one can obtain arbitrary accuracy by including higher-order eigenfunctions in the expansion

of f, Eq. (5.7). A consistent scheme for determining the expansion coefficients can be given by forming an infinite set of suitably chosen weighted averages of the boundary conditions,

$$\int_{h(\mu)>0} f(0,\mu) w_n^+ d\mu = \int_{h(\mu)>0} f_+(\mu) w_n^+ d\mu,$$
$$\int_{h(\mu)<0} f(L,\mu) w_n^- d\mu = \int_{h(\mu)<0} f_-(\mu) w_n^- d\mu, \tag{5.12}$$

where the weighting functions are $w_0^+ = w_0^- = h(\mu)$ and $w_n^\pm = f_{\pm n}(\mu)$. When the system is truncated at $n = N$ one obtains a system of $2+2N$ equations for $2 + 2N$ unknown coefficients $(\alpha, c_0, c_{\pm n})$. This method is quite general, and its potential will be demonstrated by considering two particular two-way diffusion problems. The first one is the scattering problem of Bethe *et al.*, and the other one concerns the radiative damping of a relativistic electron beam.

5.2 Electron scattering: Papers D&E

A mono-energetic beam of particles entering a medium of thickness L with heavy stationary scatterers will experience small-angle elastic scattering. This could for instance be electrons impinging on a slab of ions, since the electrons only get deflected by collisions with ions and do not change the magnitude of the velocity, as discussed in Chapter 2. Furthermore, the collision operator only contains the Lorentz operator, and the kinetic equation becomes [37]

$$\mu \frac{\partial f}{\partial z} = \mathcal{L}(f) = \frac{1}{2} \frac{\partial}{\partial \mu} (1-\mu^2) \frac{\partial f}{\partial \mu}, \tag{5.13}$$

where $f = f(z,\mu)$ is the azimuthally averaged steady-state distribution function, z is the distance of propagation (normalised with respect to the scattering length), and μ is the cosine of the pitch-angle. The appropriate boundary conditions for this problem are that a collimated beam is incident on the slab at $z = 0$ and that no particles are entering the slab from the other side at $z = L$. Mathematically, this implies that $f(0,\mu) = f_+(\mu) = \delta(\mu - 1)$ for $\mu > 0$ and $f(L,\mu) = f_-(\mu) = 0$ for $\mu < 0$, and since $h(\mu) = \mu$ the function is then specified at the correct boundaries according to Eq. (5.2).

The eigenvalue problem (5.3),

$$\frac{1}{2} \frac{\partial}{\partial \mu} (1-\mu^2) \frac{\partial f_n}{\partial \mu} = -\lambda_n \mu f_n(\mu), \tag{5.14}$$

can easily be solved numerically to give the eigenfunctions f_n. These eigenfunctions cannot, however, be expressed in a closed form in elementary functions, but approximate analytic expressions can be found. One way to do this is to optimise trial functions to satisfy a variational formulation of the eigenvalue problem (Paper E). Another way is to expand the eigenfunctions in Legendre polynomials, as is natural when the diffusion operator is of the form (5.13) (Paper D).

Knowing the eigenfunctions, the coefficients in the first-order expansion of $f(z,\mu)$,

$$\begin{aligned} f(z,\mu) \simeq\ & c_0(L)f_0 + \alpha(L)f_D(z,\mu) + \\ & + c_1(L)f_1(\mu)e^{-\lambda_1 z} + c_{-1}(L)f_{-1}(\mu)e^{-\lambda_{-1}(z-L)}, \end{aligned} \quad (5.15)$$

are determined by solving the system of equations (5.12). The improvement compared with the zeroth order expression (5.8) can be studied in terms of the particle flux. Only the diffusion solution f_D contributes to the flux integral $\Gamma = \int_{-1}^{1} f(z,\mu)\mu\, d\mu$, since integration of Eq (5.3) over the interval $[-1,1]$ shows that all the higher order eigenfunctions have vanishing flux. Thus $\alpha(L)$ determines the flux, which for $L \gg \lambda_1^{-1}$ becomes

$$\Gamma = -\frac{2}{3}\alpha(L) \simeq \frac{1.774}{1.439 + L}. \quad (5.16)$$

The flux found from the first order approximation of f and the expression (5.11) obtained by Bethe *et al.* are presented in Fig 5.1. Approximate expressions for higher order eigenfunctions ($f_2, f_3 \ldots$) can be calculated in the same manner as above. The flux found by including f_2 in the expansion of f is practically indistinguishable from the result obtained by a numerical finite difference solution of Eq. (5.13), as can be seen in Fig 5.1.

5.3 Dynamics of runaway electrons: Paper D

In a tokamak operated at low density, the electric field can be greater than the critical field, $E_\parallel > E_\mathrm{c}$. As discussed in Sec. 2.8, there is a possibility in this case that high energy electron distribution is in a steady-state. In a straight magnetic field ($R \to \infty$) the steady-state kinetic equation for the high energy electron beam is from Eq. (2.36)

$$\left(E - 1 - \frac{\hat{\tau}_{\mathrm{ee}}}{\tau_r}p_\perp^2\right)\frac{\partial f}{\partial p_\parallel} = \frac{1+Z}{2p_\perp}\frac{\partial}{\partial p_\perp}\left(p_\perp \frac{\partial f}{\partial p_\perp}\right), \quad (5.17)$$

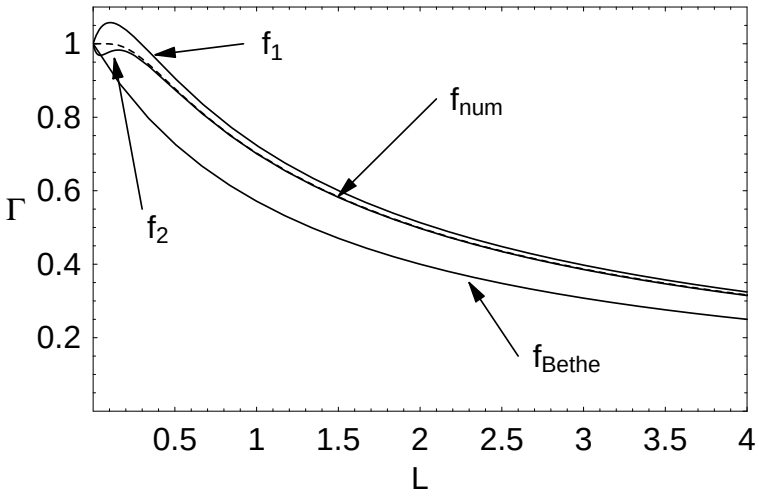

Figure 5.1: Transmission flux as a function of slab length L. The dashed line f_{num} is numerically calculated flux, f_{Bethe} is the expression found by Bethe *et al.* (Eq. (5.11)), f_1 and f_2 are the fluxes found when using the first, Eq. (5.15), and second order approximation of f, respectively.

where $E = E_\parallel/E_{\text{c}} > 1$ is the normalised parallel electric field. Equation (5.17) can be written in normalised coordinates as

$$(1-r^2)\frac{\partial f}{\partial z} = \frac{1}{r}\frac{\partial}{\partial r}r\frac{\partial f}{\partial r}, \tag{5.18}$$

where

$$p_\perp^2 = \frac{E-1}{\hat{\tau}_{\text{ee}}/\tau_r}r^2 \quad \text{and} \quad p_\parallel = \frac{2\tau_r(E-1)^2}{(1+Z)\hat{\tau}_{\text{ee}}}z. \tag{5.19}$$

Eq. (5.17) is only valid for $p_\parallel$ much larger than the critical momentum for runaway generation. The discussion in Sec. 2.8 shows that it is a complicated task to calculate the electron distribution at low $p_\parallel$ analytically. For simplicity, Paper D assumes that the runaway electron beam generated by the electric field can be modelled by a delta function in $p_\perp$ at the low $p_\parallel$ boundary of the validity region for Eq. (5.17). Furthermore, since Eq. (5.18) is translation invariant in z, it is convenient to modify the definition of z in Eq. (5.19) by an offset, so that the boundary at low $p_\parallel$ is taken to be at $z = 0$.

Eq. (5.18) should thus be solved in the domain $0 \leq z < \infty$, $0 \leq r < \infty$, and the boundary conditions are

$$\begin{aligned} f(r,z) &\to 0, & r^2+z^2 &\to \infty, \\ f(r,0) = f_+(r) &= \frac{1}{2\pi r}\delta(r), & r^2 &< 1. \end{aligned} \tag{5.20}$$

Note that boundary conditions can only be specified on the part of the $z = 0$ boundary where $h(r) = 1 - r^2 > 0$ because of the two-way nature of the equation. The coordinate r here corresponds to μ in Section 5.1.

Physically, the electrons in the runaway beam, represented by the delta function boundary condition, are accelerated by the electric field. At the same time they experience scattering, which increases their perpendicular momentum. For $r > 1$ this leads to such large emission of synchrotron radiation that the electrons are slowed down and brought back toward the low-energy boundary $z = 0$, which they cross with an unknown distribution at $r > 1$.

The theory from Section 5.1 clearly applies to Eq. (5.18). A fundamental difference, however, between this problem and that considered in the previous sections is that there is no diffusion solution of (5.18) satisfying the boundary conditions, since there is now no solution of Eq. (5.5) that vanishes at infinity. The radial eigenfunctions are found to be

$$f_n = \exp\left(-\frac{\sqrt{\gamma_n}}{2}r^2\right)\sum_{k=0}^{n} H_{2k}(r\gamma_n^{1/4})H_{2(n-k)}(0)\binom{n}{k} \tag{5.21}$$

in terms of Hermite polynomials H_k, and the eigenvalues are

$$\gamma_n = 4(2n+1)^2, \quad n = 0, 1, \dots \ . \tag{5.22}$$

The distribution function expansion (5.7) becomes

$$f(r,z) = \sum_{n=0}^{\infty} c_n f_n(r) \exp\left(-\gamma_n z\right), \tag{5.23}$$

and we observe that for large z the dominant behaviour of f is found from the eigenfunction with the lowest eigenvalue since the terms decay exponentially, $\propto \exp(-\gamma_n z)$. The expansion coefficients, c_n, are determined by solving the system of equations (5.12), i.e.

$$\int_{h(r)>0} f(r,0)\ w_n^+\ 2\pi r dr = \int_{h(r)>0} f_+(r)\ w_n^+\ 2\pi r dr, \tag{5.24}$$

with weighting functions $w_n^+ = f_n$. Since there is no diffusion solution to this problem, $h(r)$ has been excluded from the weighting functions. By numerically solving (5.24), one finds that c_0 converges towards 1.19

and the lowest order approximation of f, valid for $z \gg 1/\gamma_1 = 1/36$, becomes

$$f(r,z) \approx c_0 f_0(r) \exp\left(-\gamma_0 z\right) = 1.19 \ \exp\left(-r^2 - 4z\right). \tag{5.25}$$

When considering smaller z, higher order approximations are needed to describe f accurately. The coefficients in the next four approximations have been calculated numerically and found to be $c_1 = -0.97$, $c_2 = 0.198$, $c_3 = -0.0232$ and $c_4 = 0.0019$. Including these terms gives an accurate description of f everywhere except at very small z. In this region, $z \to 0$, the boundary condition (5.20) says nothing about the distribution function for $r > 1$, but dictates that it should be strongly peaked around $r = 0$ for $r < 1$. In fact, for $r \ll 1$, Eq. (5.18) reduces to an ordinary diffusion equation, with the solution

$$f(r,z) = \frac{1}{4\pi z} \ \exp\left(-\frac{r^2}{4z}\right). \tag{5.26}$$

Figures 5.2 and 5.3 show the truncated series solution (5.23) at $z = 0.015$ and $z = 0.06$, together with the asymptotic expressions (5.25) and (5.26). For small r the solution closely resembles Eq. (5.26), and for large r and large z it approaches Eq. (5.25). The two-way diffusion nature of the equation is also evident in Fig. 5.2; there is a population of back-scattered electrons in the region $r \sim 1.2$.

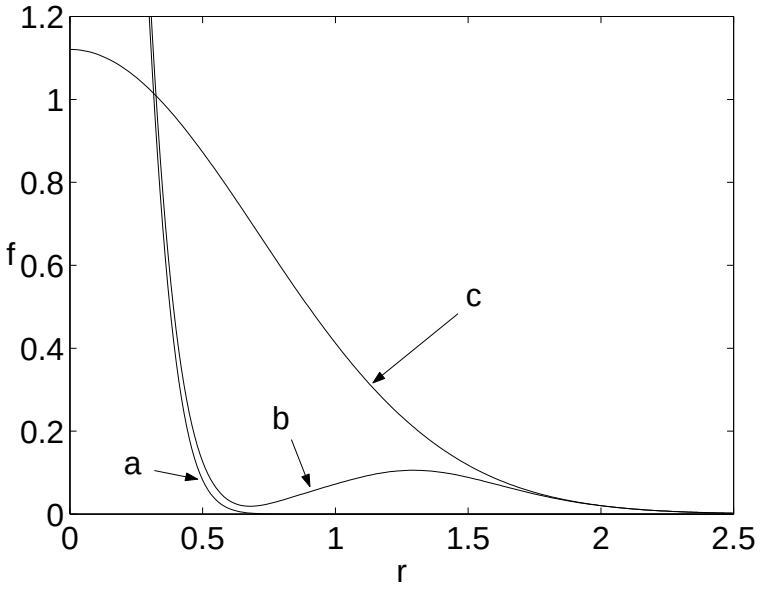

Figure 5.2: Distribution function f vs r at $z = 0.015$: (a) one-way diffusion solution (5.26); (b) series solution (5.23) truncated after terms with $n = 4$; and (c) zeroth order approximation, (5.25).

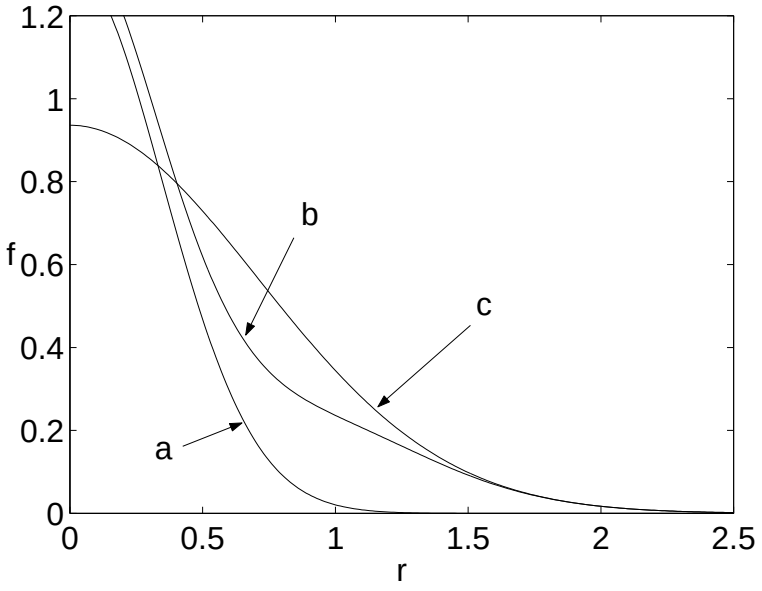

Figure 5.3: The same as Fig. 5.2 but for $z = 0.06$.

Chapter 6

Alfvén eigenmodes

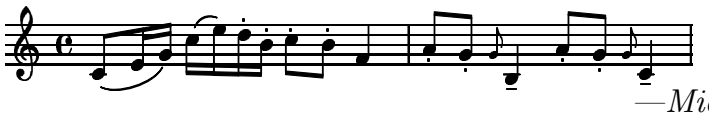

—Midsummer vigil, Hugo Alfvén

The kinetic equation and the Maxwell equations together form the basis of plasma wave theory. A simplified version of this coupled system is the cold plasma model, which is studied in this chapter with the purpose of introducing Alfvén waves and Alfvén eigenmodes.

6.1 Kinetic description and fluid closure

The kinetic description of a collisionless plasma is governed by the Vlasov equation, which describes conservation of particles in phase-space,

$$\frac{\partial f}{\partial t} + \mathbf{v} \cdot \nabla f + \frac{q}{m}(\mathbf{E} + \mathbf{v} \times \mathbf{B}) \cdot \frac{\partial f}{\partial \mathbf{v}} = 0, \tag{6.1}$$

where q and m are the particle charge and mass, respectively. The electric and magnetic fields, $\mathbf{E}$ and $\mathbf{B}$, are connected to the particle distribution function $f = f(\mathbf{x}, \mathbf{v}, t)$ through the charge density ρ and the current density $\mathbf{j}$ in the Maxwell equations. The Vlasov equation and the Maxwell equations together form a closed system, which however is too complex to be solved in general.

The system is instead reformulated in terms of the velocity moments of the distribution function. Velocity moments of the Vlasov equation provide a coupled system of evolution equations for the successive moments of f (the particle density n, the flux density $n\mathbf{v}$, the pressure

tensor $\bar{\bar{P}}$, the heat flux density $\mathbf{Q}$, etc.). If all moments could be taken into account, this system of infinitely many successively coupled differential equations would describe the macroscopic properties of a plasma completely.

The problem of how to approximate this system by truncation or by asymptotic expansion in a small parameter is called the fluid closure problem. Magnetohydrodynamics (MHD) is one of the most often used fluid closure schemes for magnetised plasmas. The simplest way to obtain fluid closure by truncation, is to neglect the pressure tensor. This is called the cold plasma model, and it can be used to describe waves and perturbations that propagate faster than the thermal speed of the plasma.

6.2 The cold plasma model

In the cold plasma approximation the particle density n_s and the flux density $n_s\mathbf{v}_s$ for particle species s are the only non-zero velocity moments of f. The two first moments of the Vlasov equation are the continuity equation and the equation of motion. The linearised momentum equation in a magnetised plasma becomes

$$m_s \frac{\partial \mathbf{v}_s}{\partial t} = q_s(\mathbf{E} + \mathbf{v}_s \times \mathbf{B}_0), \tag{6.2}$$

where equilibrium quantities are denoted with a subscript zero and perturbed quantities without a numerical subscript. The current is determined by summing the contributions from electrons and ions

$$\mathbf{J} = \sum_{s=\mathrm{e,i}} n_{0s} q_s \mathbf{v}_s. \tag{6.3}$$

Summing the momentum equations over both species, and neglecting terms of relative order $Zm_\mathrm{e}/m_\mathrm{i}$ gives

$$m_\mathrm{i} n_{0\mathrm{i}} \frac{\partial \mathbf{v}}{\partial t} = \mathbf{J} \times \mathbf{B}_0, \tag{6.4}$$

where $\mathbf{v} \simeq \mathbf{v}_\mathrm{i} + Zm_\mathrm{e}/m_\mathrm{i}\mathbf{v}_\mathrm{e}$ is the centre of mass velocity. When this is substituted back into Eq. (6.3) and into Eq. (6.2) for electrons, one obtains the generalised Ohm's law [38]

$$\mathbf{E} = -\mathbf{v} \times \mathbf{B}_0 + \frac{1}{n_\mathrm{e} e}\mathbf{J} \times \mathbf{B}_0 + \frac{m_\mathrm{e}}{n_\mathrm{e} e^2}\frac{\partial \mathbf{J}}{\partial t}. \tag{6.5}$$

The first term on the right is the electromotive force (cf. the electric field induced in a conductor moving in a magnetic field), the second term is the Hall effect, and the last term is due to electron inertia. For harmonic perturbations $\mathbf{E}, \mathbf{B} \propto \exp(-i\omega t)$, Eq. (6.5) can be written using Eq. (6.4) as

$$i\omega\epsilon_0\mathbf{E} = \frac{\omega_{\mathrm{ce}}\omega_{\mathrm{ci}}}{\omega_{\mathrm{pe}}^2}\left(-\mathbf{J}_\perp + \frac{i\omega}{\omega_{\mathrm{ci}}}\mathbf{J}\times\mathbf{b}_0 + \frac{\omega^2}{\omega_{\mathrm{ce}}\omega_{\mathrm{ci}}}\mathbf{J}\right), \tag{6.6}$$

where $\mathbf{b}_0 = \mathbf{B}_0/B_0$. In the MHD description of a plasma all fluctuations are assumed to have frequencies well below the ion cyclotron frequency ω_{ci}, which means that the last two terms can be neglected. This is the case for the Alfvén cascades studied in Chapter 8. However, for the compressional Alfvén eigenmodes in Chapter 7, ω and ω_{ci} are of the same order so the Hall term needs to be kept. Solving for $\mathbf{J}$ in equation Eq. (6.5) gives a relation

$$\mathbf{J} = \bar{\bar{\sigma}}\cdot\mathbf{E}, \tag{6.7}$$

where $\bar{\bar{\sigma}}$ is the conductivity tensor. It contains all information about the plasma response to the electric and magnetic fields, and is generally a sum of contributions from different particle species. It is sometimes more appropriate to use the dielectric tensor

$$\bar{\bar{\epsilon}} = \bar{\bar{I}} + \frac{i\bar{\bar{\sigma}}}{\epsilon_0\omega}, \tag{6.8}$$

where $\bar{\bar{I}}$ is the unity tensor. The dielectric tensor in a cold plasma is [39]

$$\bar{\bar{\epsilon}} = \begin{pmatrix} S & iD & 0 \\ -iD & S & 0 \\ 0 & 0 & P \end{pmatrix}, \tag{6.9}$$

where

$$\begin{aligned} S &= 1 + \textstyle\sum_s \dfrac{\omega_{\mathrm{p}s}^2}{\omega_{\mathrm{c}s}^2 - \omega^2} \\ D &= \textstyle\sum_s \dfrac{\omega_{\mathrm{p}s}^2}{\omega_{\mathrm{c}s}^2 - \omega^2}\dfrac{\omega_{\mathrm{c}s}}{\omega} \\ P &= 1 - \textstyle\sum_s \dfrac{\omega_{\mathrm{p}s}^2}{\omega^2}, \end{aligned} \tag{6.10}$$

and $\omega_{\mathrm{p}s}$ and $\omega_{\mathrm{c}s}$ are the plasma frequency and the cyclotron frequency of particle species s, respectively. The off-diagonal elements stem from the Hall term in Eq. (6.5).

Substituting $\mathbf{J}$ into the linearised Maxwell equations yields

$$\nabla \times \mathbf{B} = \mu_0 \mathbf{J} - i\frac{\omega}{c^2}\mathbf{E} = -i\frac{\omega}{c^2}\bar{\bar{\epsilon}} \cdot \mathbf{E} \tag{6.11}$$

$$\nabla \times \mathbf{E} = i\omega \mathbf{B} \tag{6.12}$$

Here, one has to introduce the spatial structure of the wave. The simplest case to consider is a homogeneous medium, where the general solution of a system of linear equations is a superposition of plane waves. Let $\mathbf{E}, \mathbf{B} \propto \exp(i\mathbf{k} \cdot \mathbf{x} - \omega t)$, with frequency ω and wave vector $\mathbf{k}$. In a straight magnetic field, the equations (6.11) and (6.12) become

$$\mathbf{k} \times \mathbf{B} = -\frac{\omega}{c^2}\bar{\bar{\epsilon}} \cdot \mathbf{E} \tag{6.13}$$

$$\mathbf{k} \times \mathbf{E} = \omega \mathbf{B} \tag{6.14}$$

Eliminating $\mathbf{B}$ from Eqs. (6.13) and (6.14), we obtain

$$\mathbf{k} \times (\mathbf{k} \times \mathbf{E}) + \frac{\omega^2}{c^2}\bar{\bar{\epsilon}} \cdot \mathbf{E} \equiv \frac{\omega^2}{c^2}\bar{\bar{\Lambda}} \cdot \mathbf{E} = 0. \tag{6.15}$$

For nontrivial solutions, the determinant of the matrix $\bar{\bar{\Lambda}}$ must be zero, which yields the dispersion relation

$$D(\omega, \mathbf{k}) = \det[\bar{\bar{\Lambda}}] = \det[\mathbf{nn} - \bar{\bar{I}}n^2 + \bar{\bar{\epsilon}}] = 0, \tag{6.16}$$

where $\mathbf{n} = \mathbf{k}c/\omega$ is the refractive index.

However, a tokamak plasma is not a homogeneous medium in a straight magnetic field, so the dispersion relation Eq. (6.16) can only be used locally. Globally, the geometry of the torus makes waves with perturbed field quantities proportional to $\exp i(m\theta - n\phi - \omega t)$ possible, where ϕ is the toroidal angle and θ is the poloidal angle. For fixed n and m, the dispersion relation generally gives a radially dependent ω, so there is a continuum of possible wave frequencies in the plasma. The radial dependence of ω leads to dissipation of energy through phase mixing between nearby flux surfaces, a phenomenon called continuum damping. Most waves are easily damped by this mechanism, but some discrete eigenmodes may be more persistent. The eigenmodes are determined by Eqs. (6.11) and (6.12) together with the density profile and the shape of the magnetic field. Each eigenmode has a certain frequency, and a given spatial dependence of the perturbed field amplitude.

There are several reasons why eigenmodes can start to grow in amplitude. Many of these cannot be described by the cold plasma model

but needs a kinetic treatment. For Alfvén eigenmodes the reason for the growth is often a subpopulation of energetic ions present in the tokamak due to neutral beam injection (NBI), ion cyclotron resonance heating (ICRH), or as alpha particles produced in the D–T fusion reactions. The resulting non-monotonic velocity dependence, velocity space anisotropy or spatial inhomogeneity of the energetic ion distribution function constitutes sources of free energy, that can make eigenmodes grow. The contribution to the dielectric tensor from the energetic ions in this case makes the mode frequency complex $\omega = \omega_r + i\gamma$ with $\gamma > \gamma_\mathrm{d}$, and the eigenmode is then linearly unstable with the growth rate $\gamma - \gamma_\mathrm{d} > 0$, where γ_d is a damping rate.

6.3 Alfvén waves and eigenmodes

There exists a rich variety of waves that can be described by the cold plasma model. Of particular interest for the present thesis are the Alfvén waves, which are low frequency waves ($\omega \ll \omega_\mathrm{pe}$), implying that the parallel electric field is approximately zero, since $P \simeq -\infty$ in Eq. (6.10).

The shear Alfvén wave [40] has the local dispersion relation $\omega^2 = k_\parallel^2 v_\mathrm{A}^2$, where $v_\mathrm{A} = B_0/\sqrt{\mu_0 \rho}$ is the Alfvén velocity and ρ is the mass density. The perturbed velocity $\mathbf{v}$ is perpendicular to both $\mathbf{B}_0$ and $\mathbf{k}$, reflecting the fact that the wave is incompressible. In a tokamak plasma $k_\parallel = (m - nq)/(qR)$, where q is the safety factor, and shear Alfvén waves may exist for instance as toroidicity-induced Alfvén eigenmodes (TAE) [41], global shear Alfvén eigenmodes (GAE) [42], or Alfvén cascades (AC) [43]. TAEs can exist because they reside at a discrete eigenmode frequency $\omega = v_\mathrm{A}/(2qR)$ inside a gap in the shear Alfvén continuum, thereby avoiding the strong continuum damping. The gap is caused by a toroidal coupling between the m and $m+1$ branches of the continuum near the radius where $m + 1/2 = nq(r)$. GAEs on the other hand avoid damping because their eigenfrequency is slightly lower than the minimum of the continuum. Alfvén cascades are associated with a mode of operation of the tokamak where $q(r)$ has a minimum at some radius $r_\star$. This corresponds to a toroidal current density with a maximum at a non-zero radius $r < r_\star$. The AC frequency is shifted an increment $\Delta\omega$ up from the maximum frequency $\omega_\star = v_\mathrm{A}|m/q_\star - n|/R$ of the continuum at $r = r_\star$. In Chapter 8 nonlinear second harmonic generation of ACs is investigated.

The compressional Alfvén wave, also known as the fast magnetosonic

wave, has the dispersion relation $\omega^2 = k^2 v_\mathrm{A}^2$ and the perturbed velocity vector $\mathbf{v}$ lies in the plane spanned by $\mathbf{B}_0$ and $\mathbf{k}$. Eigenmodes of these waves localised to the outboard side of the torus are the topic of Chapter 7.

Chapter 7

Compressional Alfvén eigenmodes

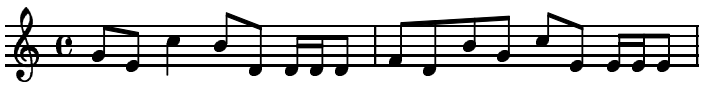

—Roslagsvår, Hugo Alfvén

The development of the theory for radial and poloidal localisation of CAE is discussed in this chapter, and the results from Paper F for the case of spherical tokamaks are presented.

7.1 Ion cyclotron emission and localised CAE

Superthermal ion cyclotron emission (ICE) has been observed in experiments at harmonics of the fast ion cyclotron frequency, evaluated in the outer midplane edge plasma. These observations were made for example in The Tokamak Fusion Test Reactor (TFTR) [44], JET [45, 46], and Japan Atomic Energy Research Institute Tokamak-60 Upgrade (JT-60U) [47]. As found in Refs. [48, 49] the emission originates from CAE, exited by energetic ions.

The localisation of the CAE to the edge of the plasma was initially investigated in Refs. [50, 51] assuming large aspect ratio and frequencies much higher than the ion cyclotron frequency. Detailed studies in the limit of circular cross section and infinite aspect ratio (*i.e.* a straight cylinder) [52,53] has shown that the inclusion of the Hall term affects the mode solutions and introduces a dependence on the sign of the poloidal phase velocity. The two-dimensional structure of the eigenmodes has

been analysed [54–57], and it was found that the eigenmodes are localised both radially and poloidally to the outboard side of the torus.

A simple explanation for the phenomenon of CAE localisation can be outlined as follows. The simple local dispersion relation $\omega^2 = v_{\mathrm{A}}^2 k^2$ can, under conditions where the equilibrium density and magnetic field are nonuniform, be generalised to $\omega^2 = -v_{\mathrm{A}}^2 \nabla^2$. Assume that a perturbed quantity X can be written $X = \hat{X}(r,\theta) \exp i(k_\theta r\theta + k_\varphi R\varphi - \omega t)$. The generalised dispersion relation indicates that the eigenmode equation takes the form

$$\left(\nabla^2 - k_\theta^2 - k_\varphi^2 + \frac{\omega^2}{v_{\mathrm{A}}^2}\right) \hat{X}(r,\theta) = 0, \tag{7.1}$$

where the toroidal wave vector is $k_\varphi = -n/R$ and n is an integer. If the eigenmode is poloidally localised, k_θ on the other hand is not given by m/r with an integer m. Instead the assumption $k_\perp \gg k_\parallel$ implies that $k_\theta \simeq nq/r$. It is now seen from Eq. (7.1) that the quantity

$$k_\theta^2 + k_\varphi^2 - \frac{\omega^2}{v_{\mathrm{A}}^2} \simeq \frac{n^2 q^2}{r^2} - \frac{\omega^2}{v_{\mathrm{A}}^2} \tag{7.2}$$

plays the role of a potential for the eigenmode problem. Because of the R and r dependence of v_{A} it can be shown that for relevant equilibrium profiles the potential has a minimum on the low field side near the plasma edge, which leads to the radial and poloidal localisation of the CAE.

7.2 Localisation of CAE in spherical tokamaks: Paper F

Spherical tokamaks, such as the Mega-Ampere Spherical Tokamak (MAST) and the National Spherical Tokamak Experiment (NSTX) have a small aspect ratio and a large ellipticity of the plasma cross section. In NSTX, emission was observed below the ion cyclotron frequency, see Fig. 7.1 [58]. It was deduced from measurements of the wave polarisation and from the strong correlation between the measured frequency and the Alfvén velocity that the emission originated from compressional Alfvén waves [58, 59]. Paper F shows that CAEs can be localised in the NSTX plasma configuration and may indeed have frequencies below f_{ci}. Experimental observations of CAEs below f_{ci} have later also been made in MAST [60] and DIII-D [61].

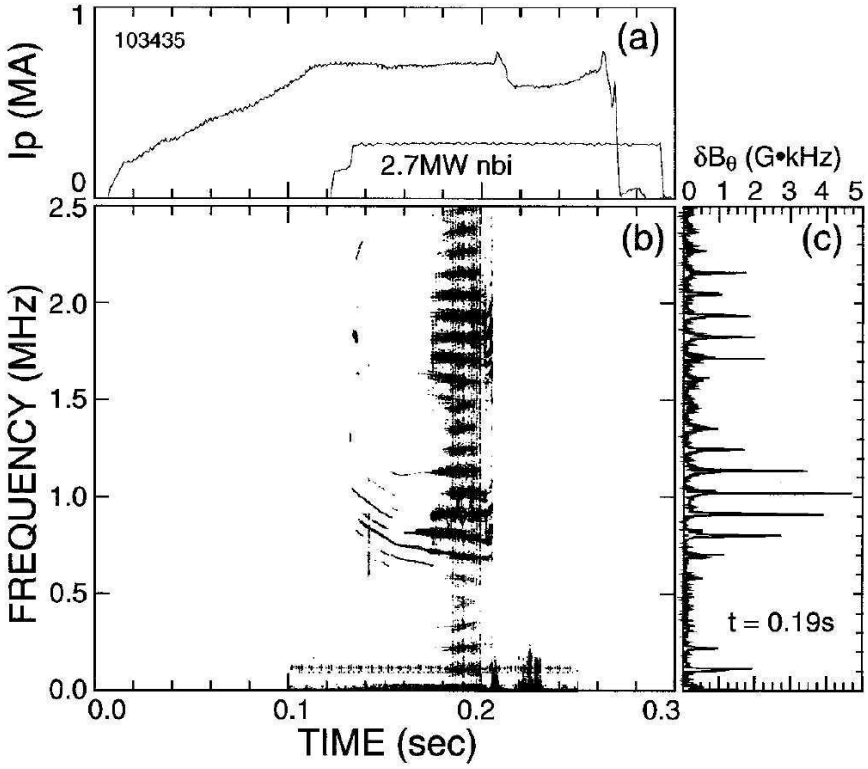

Figure 7.1: The plasma current, NBI heating power, and magnetic spectrum in NSTX discharge 103435. (Reproduced from Ref. [58])

In Paper F, compressional Alfvén waves with small parallel wave vector ($k_{\|} \ll k_{\perp}$) and with the wave frequency in the range $\omega \sim \omega_{\mathrm{ci}}$ are considered in a cold, inhomogeneous and magnetised plasma with one ion species. To capture the ellipticity of the flux surfaces and the plasma density profile in the wave field ansatz, it is appropriate to use elliptic-toroidal coordinates, defined by

$$\begin{cases} x = (R_0 + \rho\cos\vartheta)\sin\varphi \\ y = (R_0 + \rho\cos\vartheta)\cos\varphi \\ z = \kappa\rho\sin\vartheta, \end{cases} \tag{7.3}$$

where the flux label ρ is a modified radial coordinate, ϑ is the modified poloidal angle, φ is the ordinary toroidal angle, R_0 is the major radius of the torus, and κ is the ellipticity of the cross section. In NSTX, $R_0 = 85$ cm, the minor radius is $a = 65$ cm and $\kappa = 1.6$. The perturbed wave quantities X are expressed using a ballooning representation

$$X(\rho,\vartheta) = \sum_{j=-\infty}^{\infty} \hat{X}(\rho,\vartheta+2\pi j)e^{i(nq(\rho)(\vartheta+2\pi j)-n\varphi-\omega t)}, \tag{7.4}$$

where $q(\rho)$ is the safety factor and it is assumed that $j = 0$ is the dominant component. In the following, the notation of Paper F, where Gaussian units are used, is going to be employed.

An eigenmode equation can be obtained from the Maxwell equations (6.11) and (6.12) using the dielectric tensor expressed in the elliptic-toroidal coordinate system (7.3). The dielectric tensor is presented in Eq. (7.25) in Appendix 7.A, where it assumed that $(Rq/\rho\kappa)^2 \gg 1$. The parallel electric field is prescribed to be zero $E_\varphi + E_\vartheta/q = 0$, which makes it possible to eliminate the electric field components in the Maxwell equations and reduce the system to one eigenmode equation for the toroidal magnetic field amplitude $\hat{B}(\rho, \vartheta)$. Under the assumptions that n and q'/q^2 are low and the characteristic radial and poloidal length scales of the amplitude variation are sufficiently large, the eigenmode equation can be written as

$$\frac{ic}{\omega}\left\{\frac{\partial}{\partial\rho}\left[\frac{1}{c_n}\left(a_3\frac{\partial\hat{B}}{\partial\rho}+a_1\frac{\partial\hat{B}}{\partial\vartheta}\right)\right]+\frac{\partial}{\partial\vartheta}\left[\frac{1}{c_n}\left(a_4\frac{\partial\hat{B}}{\partial\rho}+a_2\frac{\partial\hat{B}}{\partial\vartheta}\right)\right]+\right.$$
$$\left.+\frac{in\vartheta q'}{c_n}\left[2a_3\frac{\partial\hat{B}}{\partial\rho}+(a_1+a_4)\frac{\partial\hat{B}}{\partial\vartheta}\right]+\frac{inq}{c_n}\left[(a_1+a_4)\frac{\partial\hat{B}}{\partial\rho}+2a_2\frac{\partial\hat{B}}{\partial\vartheta}\right]\right\}+$$
$$+V(\rho,\vartheta)\hat{B}=0, \tag{7.5}$$

where $c_n = a_1a_4 - a_2a_3$ is the determinant of the matrix

$$\begin{pmatrix} a_1 & a_2 \\ a_3 & a_4 \end{pmatrix} \simeq \epsilon_{xx}\frac{\omega}{c}\begin{pmatrix} -R\omega/\omega_{\mathrm{ci}} - i\sqrt{g}g^{\rho\vartheta} & -i\sqrt{g} - g^{\vartheta\vartheta} \\ -i\sqrt{g}g^{\rho\rho} & R\omega/\omega_{\mathrm{ci}} - i\sqrt{g} - g^{\vartheta\rho} \end{pmatrix}. \tag{7.6}$$

Here $R = R_0 + \rho\cos\vartheta$ is the distance to the major axis of the torus, $g = \det g_{ij}$ is the determinant of the metric tensor given by Eq. (7.17), and $\epsilon_{xx} = \omega_{\mathrm{pi}}^2/(\omega_{\mathrm{ci}}^2 - \omega^2)$. The real part of the potential $V(\rho, \vartheta)$ is

$$H(\rho,\vartheta) = \mathrm{Re}\{V\} = \frac{\sqrt{g}}{R^2} - n^2\left[q^2g^{\vartheta\vartheta} + 2qq'\vartheta g^{\rho\vartheta} + (q')^2\vartheta^2g^{\rho\rho}\right]\frac{v_{\mathrm{A}}^2\sqrt{g}}{\omega^2R^2} +$$
$$+\frac{n}{\omega}\left(q\frac{\partial}{\partial\rho} - \vartheta q'\frac{\partial}{\partial\vartheta}\right)\left(\frac{v_{\mathrm{A}}^2}{R\omega_{\mathrm{ci}}}\right). \tag{7.7}$$

In Eq. (7.5), toroidal effects have been included in v_{A} and ω_{ci} through the poloidal dependence of the equilibrium magnetic field, which is assumed to fall off as $1/R$. The term in H involving derivatives with respect to ρ and ϑ originates from the Hall term, which has been included in the infinite aspect ratio limit in Refs. [52, 53, 55]. This term,

which is large at the edge where the gradient of the plasma density is large, breaks the poloidal symmetry even when the inverse aspect ratio is small.

Using Hermite functions $h_s(x) = H_s(x)e^{-x^2/2}$, an ansatz can be made for the field amplitude of the form

$$\hat{B}(\rho,\vartheta) = B_0 h_s(\frac{\rho-\rho_0}{\Delta})h_p(\frac{\vartheta-\vartheta_0}{\eta}) \ , \tag{7.8}$$

where the simplest case $s = p = 0$ corresponds to a Gaussian variation of the amplitude. A variational formulation of Eq. (7.5) is then used to determine the localisation radius ρ_0, the radial localisation width Δ, the localisation angle ϑ_0, the poloidal localisation width η, and the eigenmode frequency ω. Figure 7.2 shows ρ_0 and ω from numerical solutions of the variational equations. It is found that the solutions for higher toroidal mode numbers are generally better localised. Because of the Hall term, the solutions are not symmetrical with respect to the sign of the toroidal mode number; no numerical solutions were found for $n > 0$. Neglecting the Hall term, the eigenfrequency is found analytically to be

$$\omega_{|n|,s,p} \simeq \frac{v_\mathrm{A}}{\rho_0}\sqrt{\frac{n^2q^2}{\kappa^2} + k_p + \frac{|n|q}{\kappa}\alpha_{sp}} \ , \tag{7.9}$$

where k_p and α_{sp} are

$$\begin{aligned} k_p &= (1-\kappa^{-2})(10p^2-2p+3)/4 \\ \alpha_{sp} &= (2s+1)(\rho_0/R)\sqrt{1+(3+R_0/\rho_0)^2} + \\ &\quad +(2p+1)\sqrt{1-R_0/(\kappa^2 R)}. \end{aligned} \tag{7.10}$$

The experimentally observed emission peaks of the NSTX discharge 103701 appear in two bands, spanning $0.7-1.2$ MHz and $1.5-2.2$ MHz. At the edge the ion cyclotron frequency is $f_\mathrm{ci} = 2.3$ MHz. The detected peaks are separated by a spacing of about 120 kHz $\simeq 0.05 f_\mathrm{ci}$ and each peak has a number of surrounding subpeaks separated by about 20 kHz.

The approximate eigenfrequencies in Eq. (7.9) and the numerical results presented in Fig. 7.2 are in the same range as the observed bands. However, the frequency splittings between successive mode numbers (n and $n+1$, s and $s+1$ etc.) do not agree with the experimentally measured 120 kHz or 20 kHz. In a recent study of the CAE eigenmode problem using a numerical MHD code (without the Hall term) detailed calculations of the eigenmode structure were made and the corresponding frequency splittings were found to agree better with experiments [62].

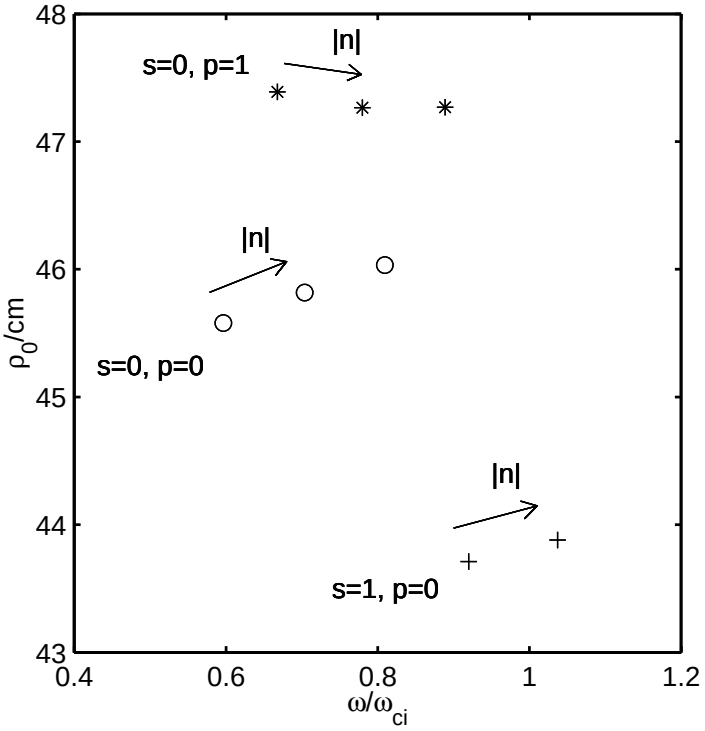

Figure 7.2: Solutions of the variational equations for the three cases $\{s = 0,\ p = 0\}$ (a Gaussian magnetic field ansatz), $\{s = 1,\ p = 0\}$, and $\{s = 0,\ p = 1\}$. The arrows for $|n|$ start at the solution where $n = -4$ and point towards higher $|n|$, except for $\{s = 1,\ p = 0\}$, where it starts at $n = -5$. For $\{s = 1,\ p = 0,\ n = -4\}$ no solution was found.

For comparison with the NSTX experimental data, apart from wave localisation, a complete analysis should also include the resonant interaction between fast ions and CAE, where the resonance condition needs to be satisfied and a positive growth rate has to be found. These aspects were not investigated in Paper F. Later research in this field [63] has shown that the observed spectrum in NSTX is caused by both CAE and GAE.

Appendix 7.A: The dielectric tensor in elliptic-toroidal coordinates

This appendix is included here, because it clarifies the results presented in the Appendix of Paper F. In a spherical tokamak, it is suitable to use the elliptic-toroidal coordinates defined in Eq. (7.3). The covariant and contravariant base vectors are [64]

$$\mathbf{e}_\rho = (\cos\vartheta\sin\varphi, \cos\vartheta\cos\varphi, \kappa\sin\vartheta) \tag{7.11}$$
$$\mathbf{e}_\vartheta = \rho(-\sin\vartheta\sin\varphi, -\sin\vartheta\cos\varphi, \kappa\cos\vartheta) \tag{7.12}$$
$$\mathbf{e}_\varphi = R(\cos\varphi, -\sin\varphi, 0) \tag{7.13}$$
$$\mathbf{e}^\rho = (\cos\vartheta\sin\varphi, \cos\vartheta\cos\varphi, \kappa^{-1}\sin\vartheta) \tag{7.14}$$
$$\mathbf{e}^\vartheta = \frac{1}{\rho}(-\sin\vartheta\sin\varphi, -\sin\vartheta\cos\varphi, \kappa^{-1}\cos\vartheta) \tag{7.15}$$
$$\mathbf{e}^\varphi = \frac{1}{R}(\cos\varphi, -\sin\varphi, 0), \tag{7.16}$$

where $R = R_0 + \rho\cos\vartheta$. Note that this coordinate system is not orthogonal. The covariant metric tensor is [65]

$$[g_{ij}] = \begin{pmatrix} \cos^2\vartheta + \kappa^2\sin^2\vartheta & \rho\sin\vartheta\cos\vartheta(\kappa^2-1) & 0 \\ \rho\sin\vartheta\cos\vartheta(\kappa^2-1) & \rho^2(\kappa^2\cos^2\vartheta + \sin^2\vartheta) & 0 \\ 0 & 0 & R^2 \end{pmatrix}. \tag{7.17}$$

The Jacobian J is the square root of the determinant g of the covariant metric tensor, $J = \sqrt{g} = \kappa\rho R$.

To express the conductivity tensor in this coordinate system one can start by constructing a local Cartesian system with the coordinate z along the magnetic field, *i.e.* $\hat{z} \| \mathbf{B}_0$. The basis vectors of such a system are

$$\hat{x} = \mathbf{e}^\rho/|\mathbf{e}^\rho| = \frac{\sqrt{g}}{R\sqrt{g_{\vartheta\vartheta}}}\mathbf{e}^\rho \tag{7.18}$$
$$\hat{y} = \hat{z}\times\hat{x} = \frac{\sqrt{g_{\vartheta\vartheta}}}{R\sqrt{q^2R^2 + g_{\vartheta\vartheta}}}(qR^2\frac{g_{\rho\vartheta}}{g_{\vartheta\vartheta}}\mathbf{e}^\rho + qR^2\mathbf{e}^\vartheta - R^2\mathbf{e}^\varphi) \tag{7.19}$$
$$\hat{z} = \frac{\mathbf{e}_\varphi + \mathbf{e}_\vartheta/q}{|\mathbf{e}_\varphi + \mathbf{e}_\vartheta/q|} = \frac{1}{\sqrt{q^2R^2 + g_{\vartheta\vartheta}}}(g_{\rho\vartheta}\mathbf{e}^\rho + g_{\vartheta\vartheta}\mathbf{e}^\vartheta + qR^2\mathbf{e}^\varphi) \tag{7.20}$$

Next, the conductivity tensor is transformed from this system to the curvilinear coordinates. The known conductivity tensor in a Cartesian

system is obtained from Eqs. (6.8) and (6.10) and it has the elements

$$\sigma_{xx} = \sigma_{yy} = -i\epsilon_0\omega(S-1) \tag{7.21}$$

$$\sigma_{xy} = -\sigma_{yx} = \epsilon_0\omega D \tag{7.22}$$

$$\sigma_{zz} = -i\epsilon_0\omega(P-1). \tag{7.23}$$

After transformation to the elliptic-toroidal coordinate system, the contravariant conductivity tensor is found to be

$$\sigma^{ij} = \begin{pmatrix} \sigma_{xx}g^{\rho\rho} & \sigma_{xx}g^{\rho\vartheta} + \sigma_{xy}cqd & -\sigma_{xy}g^{\rho\rho}c/d \\ \sigma_{xx}g^{\rho\vartheta} - \sigma_{xy}cqd & \sigma_{xx}g^{\vartheta\vartheta} + c^2 f & -\sigma_{xy}g^{\rho\vartheta}c/d + qc^2 f \\ \sigma_{xy}g^{\rho\rho}c/d & \sigma_{xy}g^{\rho\vartheta}c/d + qc^2 f & \sigma_{xx}g^{\varphi\varphi} + q^2c^2 f \end{pmatrix}, \tag{7.24}$$

where $1/c^2 = q^2R^2 + g_{\vartheta\vartheta}$, $d = R/(\rho\kappa)$, and $f = \sigma_{zz} - \sigma_{xx}$. If zero parallel electric field $E_\varphi + E_\vartheta/q = 0$ is prescribed, the value of σ_{zz} is of no importance to the calculation of the current, and it can arbitrarily be set to σ_{xx} to simplify the expression above. Note that in the Appendix of Paper F, it is stated that σ_{zz} is really equal to σ_{xx}, which is incorrect. Finally, the assumption $(Rq/\rho\kappa)^2 \gg 1$ allows the conductivity tensor to be approximated by

$$\sigma^{ij} = \begin{pmatrix} \sigma_{xx}g^{\rho\rho} & \sigma_{xx}g^{\rho\vartheta} + \sigma_{xy}/(\rho\kappa) & 0 \\ \sigma_{xx}g^{\rho\vartheta} - \sigma_{xy}/(\rho\kappa) & \sigma_{xx}g^{\vartheta\vartheta} & 0 \\ 0 & 0 & \sigma_{xx}g^{\varphi\varphi} \end{pmatrix}. \tag{7.25}$$

Chapter 8

Alfvén cascades

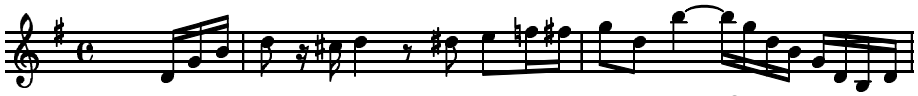

—Vallflickans dans, Hugo Alfvén

An introduction to Alfvén cascades is given in this chapter, and the eigenmode equation is presented. The theory developed in Paper G for nonlinear generation of a second harmonic of the AC perturbation, is discussed in the last section.

8.1 Alfvén cascade eigenmodes

In steady-state operation of a future fusion reactor the toroidal current will have to be generated non-inductively, and the maximum current density is not expected to appear on the magnetic axis. This implies that the magnetic shear $s = r/q\, dq/dr$ (where q is the safety factor) is negative in the plasma centre. Such modes of operation (called *reversed shear* or *optimised shear* operation) have been investigated in many tokamaks, both because they are reactor relevant and because regions of quite a flat q-profile are beneficial for producing internal transport barriers.

Alfvén cascades were first found in reversed shear operation of JT-60U [66], but the observations were initially interpreted as TAEs. ACs have later been observed in JET [67], TFTR [68], DIII-D [69], Alcator C-Mod [70], and MAST [71]. A theoretical explanation was given in Refs. [43, 72], where it was found that the eigenmodes are localised around the radius $r_\star$ where $q(r)$ has its minimum value $q(r_\star) = q_\star$. The

name Alfvén cascades originates from the characteristic rapid upward sweeping of the mode frequency due to the decrease of $q_\star$ during the current ramp-up phase. Some authors instead prefer to use the term reversed shear Alfvén eigenmodes (RSAEs) [73, 74]. ACs are of interest in magnetic fusion research for several reasons. One reason is the possibility to use them as a diagnostic tool to aid in the determination of the q profile [72]. Another issue relevant for most eigenmodes excited by energetic particles is whether the modes affect the confinement of the fast particles [75, 76]. Of particular concern is the confinement of energetic alpha particles in future fusion reactors.

ACs are excited by energetic particles (NBI or ICRH generated fast ions in JET and JT60-U, fusion generated alpha particles in TFTR), and they also belong to a class of eigenmodes called energetic particle modes (EPMs) [77], in the sense that they are dependent on the non-perturbative energetic particle response for the very existence of the eigenmode structure. For ACs, the fast particles shift the eigenmode frequency an increment $\Delta\omega > 0$ away from the local maximum of the shear Alfvén continuum $\omega_\star = |m/q_\star - n|\, v_\mathrm{A}/R$ at the minimum q surface, and continuum damping is thereby avoided. During current ramp-up, $q_\star$ falls and the AC frequency rises until it reaches the frequency of the TAE gap, where the eigenmode is converted into a TAE. The theory for this conversion is given in Ref. [78], where it is found that the toroidal coupling to neighbouring poloidal harmonics also affects the value of the frequency shift $\Delta\omega$ and thus the condition for mode existence.

8.2 The eigenmode equation

The derivation of the AC eigenmode equation is a first order perturbation analysis starting with the linearisation of all variables $\mathbf{J} = \mathbf{J}_0 + \mathbf{J}_1$, $\mathbf{B} = \mathbf{B}_0 + \mathbf{B}_1$, $\mathbf{E} = \mathbf{E}_1$, $\mathbf{v} = \mathbf{v}_1$, where the subscript zero designates equilibrium quantities. The perturbations are small ($\mathbf{B}_1 \ll \mathbf{B}_0$ etc.) and have a single harmonic temporal evolution $\propto e^{-i\omega t}$. The perturbed electric and magnetic fields are expressed in the perturbed scalar and vector potentials V and $\mathbf{A}$ as

$$\mathbf{E} = -\nabla V - \frac{1}{c}\dot{\mathbf{A}}, \quad \mathbf{B}_1 = \nabla \times \mathbf{A}, \tag{8.1}$$

where the overhead dot denotes partial time derivative. For MHD waves, the assumption $\mathbf{E}_\parallel = 0$ implies that $i\omega \mathbf{A}_\parallel = c\mathbf{b}_0\, \mathbf{b}_0 \cdot \nabla V$, so

$$\mathbf{E} = -\nabla_\perp V + \frac{i\omega}{c}\mathbf{A}_\perp, \tag{8.2}$$

where $\nabla_\perp V = \nabla V - \mathbf{b}_0\, \mathbf{b}_0 \cdot \nabla V$. To conform to the notation used in Paper G, introduce $V = \dot{\Phi}_1$ and $\mathbf{A}_\perp = c\nabla\Psi_1 \times \mathbf{b}_0$. The velocity perturbation is given by

$$\mathbf{v}_1 = \frac{\mathbf{E} \times \mathbf{B}_0}{B_0^2} = \frac{\mathbf{b}_0}{B_0} \times \nabla\dot{\Phi}_1 + \frac{1}{B_0}\nabla_\perp \dot{\Psi}_1. \tag{8.3}$$

The Ψ_1 term, which has a component along the wave vector, is associated with the compressional perturbation, whereas the incompressible shear Alfvén wave is described by the scalar Φ_1.

The eigenmode equation is derived from the momentum balance equation,

$$\rho\frac{d\mathbf{v}}{dt} = \frac{1}{c}\mathbf{J} \times \mathbf{B} - \nabla \cdot \bar{\bar{P}}, \tag{8.4}$$

which includes a contribution from the fast particles through the anisotropic part of the pressure tensor $\bar{\bar{P}}$ [79]. It is assumed that $\beta = p/(B_0^2/2\mu_0)$ is low, so background plasma contributions to the pressure tensor will be neglected. The incompressible perturbation Φ_1 is obtained by vector multiplying the linearised version of Eq. (8.4) by $\mathbf{b}_0/B_0$ and taking the divergence, which gives the *vorticity* equation. If one further assumes a large aspect ratio cylindrical solution $\Phi_1 = \tilde{\Phi}_1(r)e^{i(n\varphi - m\theta - \omega t)}$ with $m \gg 1$ and neglects toroidal coupling to $m \pm 1$ modes, the eigenmode equation becomes [43]

$$\frac{1}{r}\frac{d}{dr}\left(rD\frac{d\tilde{\Phi}_1}{dr}\right) - \frac{m^2}{r^2}D\tilde{\Phi}_1 = \frac{4\pi e}{c\bar{B}_0}\frac{m}{r}\tilde{\Phi}_1\frac{d}{dr}\left(\omega\bar{n}_{\mathrm{hot}} - k_\parallel\frac{\bar{j}_{\parallel\mathrm{hot}}}{e}\right), \tag{8.5}$$

where $D = \omega^2/\bar{v}_{\mathrm{A}}^2 - \bar{k}_\parallel^2$ and overhead bar denotes flux surface averaging.

We now introduce a normalised coordinate $x = (r - r_\star)m/r_\star$ and Taylor expand $\bar{k}_\parallel$ around the zero shear point $r = r_\star$, so that Eq. (8.5) can be written

$$\frac{d}{dx}(S + x^2)\frac{d\tilde{\Phi}_1}{dx} - (S + x^2)\tilde{\Phi}_1 + Q\tilde{\Phi}_1 = 0, \tag{8.6}$$

where

$$S = \frac{\omega^2 - \omega_\star^2}{\omega_\star^2}\frac{mq_\star}{r_\star^2 q_\star''}(m - nq_\star), \tag{8.7}$$

and primes designate derivatives with respect to r. The coefficient Q in Eq. (8.6) originates from the right hand side of Eq. (8.5) and describes the influence of hot ions,

$$Q = -\frac{4\pi e \bar{R} q_\star^2}{c \bar{B}_0 r_\star q_\star''} \frac{\partial}{\partial r} \left(\frac{\bar{v}_{\mathrm{A}}^2 |m - n q_\star|}{m - n q_\star} \bar{n}_{\mathrm{hot}} - \frac{\bar{j}_{\parallel \mathrm{hot}}}{e} \right) \tag{8.8}$$

If toroidicity effects are also included in the derivation, one more term should be added to Eq. (8.8), see Ref. [78]. Furthermore, it has recently been shown [80,81] that when the presence of a pressure gradient is taken into account, even more terms should be included in the definition of Q. All these contributions are important for determining the existence of ACs, because Eq. (8.6) does only have eigenmode solutions when $Q > 1/4$ [43].

8.3 Second harmonic generation: Paper G

Second harmonic density fluctuations of ACs have been found in Alcator C-Mod. The measurements, presented in Fig. 8.1, were made using phase contrast imaging through the plasma core [70]. Simultaneous measurements with magnetic pick-up coils did not show any second harmonic magnetic perturbation. Figure 8.1 shows how the measured second harmonic (2ω) density signal closely follows the rapidly sweeping motion of the basic AC frequency $\omega = \omega_\star + \Delta\omega$.

Paper G investigates the possibility that this density perturbation is produced by nonlinear terms in the momentum balance and continuity equations. The nonlinearity of shear Alfvén waves is relatively weak, but on the other hand the second harmonic perturbation is amplified by being nearly resonant with the $(2n, 2m)$ branch of the Alfvén continuum. Therefore, one has to do a careful analysis of the magnetic curvature effects and coupling to compressional waves. For simplicity, we continue to use the low β assumption. However, this assumption is not valid at the lowest frequencies of the AC sweeping interval, where coupling to the acoustic wave becomes important [80], so the analysis is restricted to the upper part of the frequency span.

Paper G presents a second order perturbation analysis, where the linearised quantities are written as $\mathbf{B} = \mathbf{B}_0 + \mathbf{B}_1 + \mathbf{B}_2 + \text{c.c.}$, with $\mathbf{B}_1 \propto e^{i\omega t}$, $\mathbf{B}_2 \propto e^{i2\omega t}$, and $\mathbf{B}_0 \gg \mathbf{B}_1 \gg \mathbf{B}_2$. The velocity at the basic frequency can still be represented as in Eq. (8.3), but for this calculation Ψ_1 can be of importance. The coupling between Ψ_1 and

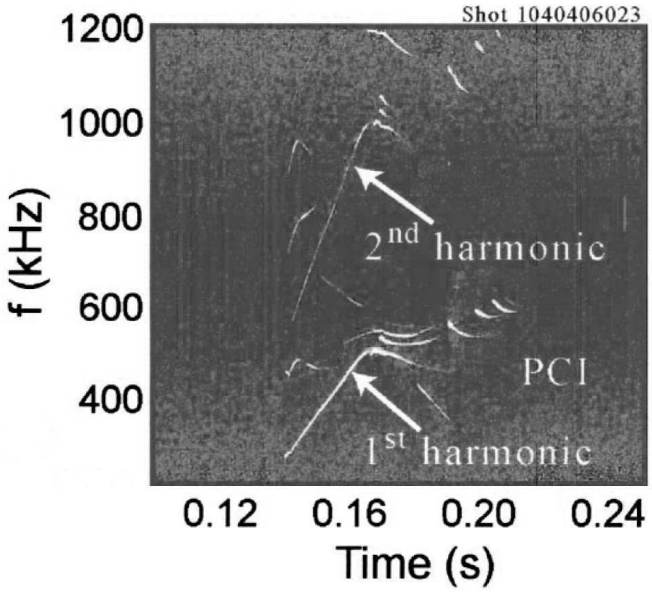

Figure 8.1: Measurements of density perturbations from Alcator C-Mod. (Reproduced from Ref. [70])

Φ_1 is determined by the *compressional* equation, which is given by the divergence of the perpendicular component of the linearised first order version of the momentum balance equation (8.4). This gives the estimate $\Psi_1 \sim \Phi_1 \epsilon^2 / m^2 q^2$.

The representation of the second harmonic velocity has to include also the possibility of a component ξ_2 along the magnetic field,

$$\mathbf{v}_2 = \xi_2 \mathbf{b}_0 + \frac{\mathbf{b}_0}{B_0} \times \nabla \dot{\Phi}_2 + \frac{1}{B_0} \nabla_\perp \dot{\Psi}_2. \tag{8.9}$$

To calculate $\mathbf{v}_2$, the momentum balance equation (8.4) is expanded to second order in the perturbed velocity. The quadratic terms in $\mathbf{v}_1$ in this second order equation will drive the second harmonic velocity through terms that are linear in $\mathbf{v}_2$. The three components of $\mathbf{v}_2$ can be determined by three different "projections" of the second order momentum balance equation. The vorticity and compressional equations determine Φ_2 and Ψ_2, respectively, and ξ_2 is obtained from the parallel component of the second order momentum balance equation. Figure 8.2 shows two examples of the radial structure of Φ_2 as calculated from the vorticity equation derived in Paper G.

Once $\mathbf{v}_1$ and $\mathbf{v}_2$ have been derived, the second harmonic density perturbation ρ_2 (the experimentally measured quantity) can be determined from the first and second harmonic components of the continuity

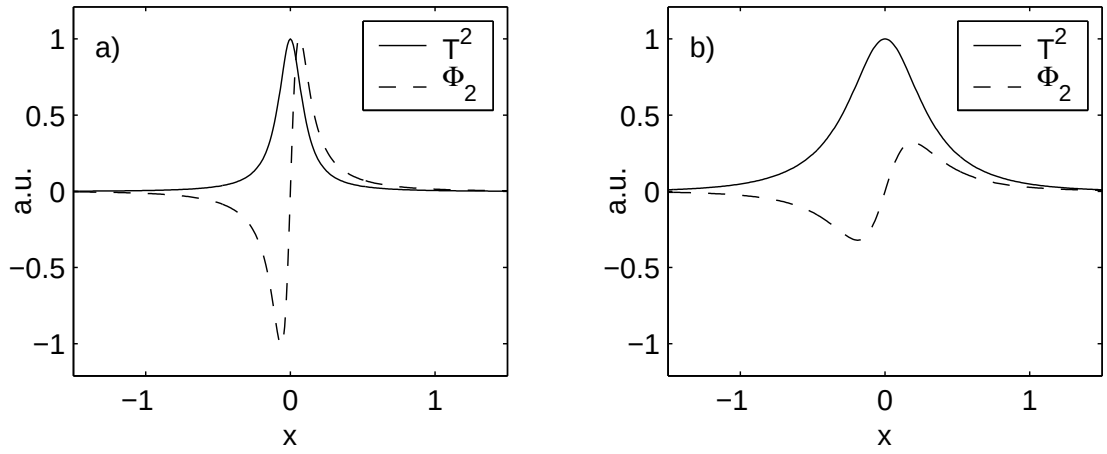

Figure 8.2: The radial envelope of the second harmonic shear perturbation Φ_2 is generated by the first harmonic shear perturbation [here normalised to $T(x) = m\tilde{\Phi}_1/(r_\star\sqrt{\bar{B}_0})$] through the second harmonic vorticity equation. These calculations have been made for the lowest-order radial eigenmode solution to Eq. (8.6) for the cases (a) $Q = 0.65$, $S = 0.011$ and (b) $Q = 1$, $S = 0.1$.

equation,

$$\dot{\rho}_1 = -\nabla \cdot (\rho_0 \mathbf{v}_1), \tag{8.10}$$

$$\dot{\rho}_2 = -\nabla \cdot (\rho_1 \mathbf{v}_1) - \nabla \cdot (\rho_0 \mathbf{v}_2). \tag{8.11}$$

It turns out that the first term in Eq. (8.11) is dominated by contributions proportional to Φ_1^2 and the second term is dominated by Φ_2, so the compressional perturbation and the perturbation along the magnetic field are in fact negligible. The parameter Q defined in Eq. (8.8) determines the ordering of the two terms in Eq. (8.11). Figure 8.2 indicates that Φ_2 decreases with increasing Q. Hence, at high Q the nonlinearity of the momentum balance equation gives the most prominent contribution to ρ_2. On the other hand, when Q is low, as in Fig. 8.2a, the dominant effect is instead the nonlinearity of the continuity equation (the first term in Eq. (8.11)).

When the maximum amplitudes of the two harmonics ρ_1 and ρ_2 are compared, it is seen that in the case of low Q,

$$\frac{\rho_2}{\rho_1} \sim \frac{mq}{\epsilon}\frac{|\mathbf{B}_1|}{B_0}. \tag{8.12}$$

Measuring the density fluctuations ρ_1 using interferometry techniques is a way to obtain information about the AC amplitude inside the plasma,

instead of just at the edge as with magnetic probes. Equation (8.12) indicates that measuring ρ_2 could potentially also be helpful in diagnosing the AC inside the plasma.

Chapter 9

Conclusions and outlook

The present thesis contributes to the understanding of the phenomena of runaway electrons, two-way diffusion equations, compressional Alfvén eigenmodes, and Alfvén cascades. The conclusions are summarised below.

9.1 Runaway electrons

The kinetics of a rapidly cooling plasma and the so-called burst mechanism for runaway electron generation have been investigated. For a certain temperature evolution it was found that the velocity distribution function asymptotically approaches a self-similar solution with an extended tail. When the collision time is not very much shorter than the time scale of the thermal quench, an estimate of the number of runaway electrons shows that the runaway generation starts earlier and can be larger than predicted by ordinary Dreicer generation.

A model has been developed for the evolution of the radial current density profile in tokamak disruptions accompanied by runaway production. When primary runaway generation is small, but not negligible, resistive diffusion of electric field causes the post-disruption current density profile to become more peaked on the magnetic axis than the initial one. This may affect the stability of the post-disruption plasma. The final current profile is also very sensitive to small scale variations in the pre-disruption parameters, and it can easily become filamented. The present version of the model does not include the burst effect, because this would add the velocity space dynamics to the problem, which at present only models the evolution of the distribution function in radius

and time. In ITER, the burst mechanism is predicted to be important, so reliable predictions will presumably have to be based on simulations of the complete Fokker-Planck equation.

The dynamics of runaway electrons in tokamak discharges is described by kinetic equations of the two-way diffusion type. A general approximation scheme for solving such two-way diffusion equations has been developed and applied to two relevant cases, electron beam scattering in a slab and the formation of runaway electron tail distributions. In the latter case, the two-way solution scheme was used to determine the steady-state runaway electron beam distribution function at high energies, where synchrotron radiation and pitch-angle scattering balance the electric field. This is a relevant case for tokamaks operated at low density, where the Ohmic electric field used to drive the plasma current can be larger than the critical field, $E_\parallel > E_\mathrm{c}$.

The success of future fusion experiments depends on finding a way to prevent runaway electrons or minimising the damage they can cause. To be able to do this, it is essential to understand the generation mechanisms, and the present thesis is a step in that direction. Several methods to shut down the plasma in a controlled and safe manner have been suggested in the literature [13]. Drastically increasing the plasma density by injection of gas puffs, killer pellets, or liquid jets would increase the critical electric field and prevent runaway acceleration. The theory of Paper C provides a good tool for determining the runaway production when using such methods. In Ref. [82] the cooling and the plasma density increase due to killer pellet injection is obtained from a pellet ablation code and the runaway production is then calculated using the model in Paper C.

9.2 Alfvén eigenmodes

The emission of radiation at harmonics of the ion cyclotron frequency in large aspect ratio tokamaks has previously been shown to originate from localised compressional Alfvén eigenmodes. The mode localisation theory is extended in this thesis to the case of elliptic cross section and aspect ratio of order unity, which is typical for a spherical tokamak.

Approximate solutions to the eigenmode equation are obtained from a variational formulation of the problem. The eigenmodes are found to be localised to the outer midplane edge of the torus, and solutions with higher toroidal mode number are generally more localised. The Hall

term breaks the symmetry with respect to the sign of the toroidal mode number n, and excludes solutions for positive n. The found eigenmodes indeed have frequencies in the same range as the observed emission in NSTX, although the measured frequency splittings between successive eigenmodes is not accurately reproduced. Better agreement with the experiment in this respect has recently been obtained from detailed numerical calculations of the eigenmode structure, as reported in Ref. [62]. In a fusion reactor, the emission from CAE could become a useful tool to obtain information about the energetic alpha particle distribution. Recent observations in DIII-D have indicated that CAEs might be excited in ITER [61].

Alfvén cascades are shear Alfvén eigenmodes localised around the minimum q radius in tokamaks with reversed central shear. Second harmonic density perturbations for ACs were seen in Alcator C-Mod using the phase contrast imaging diagnostic. This motivated the development of the theory presented in this thesis for second harmonic generation through non-linear terms in the MHD equations. The perturbation at the double frequency produced by the weak quadratic non-linearity of the shear wave is enhanced by the fact that it is nearly resonant with the $(2n, 2m)$ branch of the Alfvén continuum. The present thesis shows how to determine the amplitude and the radial structure of the second harmonic perturbation. The ratio between the amplitudes of the second harmonic density perturbation and the basic frequency perturbation has been estimated. The result could potentially be used obtain information about the AC amplitude of the basic harmonic magnetic perturbation inside the plasma. However, this is complicated because of the uncertainties introduced in the phase contrast imaging measurements [83].

Other aspects of AC measurements have shown to be very suitable for diagnostic purposes. Determining the minimum of the q profile from AC observations is a useful aid in the calculation of the q profile [67]. Recently, attention has been drawn to the low frequency onset of the frequency sweep of Alfvén cascades. For these frequencies the coupling to acoustic perturbations is important, and it has been proposed that measuring the minimum frequency can be a way to determine the plasma temperature at the minimum q location [80].

References

[1] J. Wesson, *Tokamaks* (Clarendon Press, Oxford, 2004).

[2] M. Keilhacker, A. Gibson, C. Gormezano *et al.*, Nuclear Fusion **39**, 209 (1999).

[3] P. Helander and D. J. Sigmar, *Collisional Transport in Magnetized Plasmas* (Cambridge University Press, Cambridge, 2002).

[4] M. N. Rosenbluth, W. M. MacDonald, and D. L. Judd, Physical Review **107**, 1 (1957).

[5] H. Dreicer, Physical Review **115**, 238 (1959).

[6] H. Dreicer, Physical Review **117**, 329 (1960).

[7] J. W. Connor and R. J. Hastie, Nuclear Fusion **15**, 415 (1975).

[8] A. V. Gurevich, Sovjet Phys. JETP **12**, 904 (1961).

[9] M. D. Kruskal and I. B. Bernstein, Technical Report No. MATT-Q-20, Princeton Plasma Physics Laboratory (unpublished).

[10] R. H. Cohen, Physics of Fluids **19**, 239 (1976).

[11] P. Sandquist, S. E. Sharapov, P. Helander, and M. Lisak, Physics of Plasmas **13**, 072108:1 (2006).

[12] M. N. Rosenbluth and S. V. Putvinski, Nuclear Fusion **37**, 1355 (1997).

[13] V. Riccardo and JET EFDA contributors, Plasma Physics and Controlled Fusion **45**, A269 (2003).

[14] S. Putvinski, P. Barabaschi, N. Fujisawa, N. Putvinskaya, M. N. Rosenbluth, and J. Wesley, Plasma Physics and Controlled Fusion **39**, B157 (1997).

[15] S. Jardin, G. Schmidt, E. Fredrickson, K. Hill, J. Hyuna, B. Merrill, and R. Sayer, Nuclear Fusion **40**, 923 (2000).

[16] R. W. Harvey, V. S. Chan, S. C. Chiu, T. E. Evans, M. N. Rosenbluth, and D. G. Whyte, Physics of Plasmas **7**, 4590 (2000).

[17] K. H. Finken, G. Mank, A. Krämer-Flecken, and R. Jaspers, Nuclear Fusion **41**, 1651 (2001).

[18] D. G. Whyte, T. C. Jernigan, D. A. Humphreys *et al.*, Physical Review Letters **89**, 055001:1 (2002).

[19] E. M. Hollman, T. C. Jernigan, M. Groth *et al.*, Nuclear Fusion **45**, 1046 (2005).

[20] M. Bakhtiari, H. Tamai, Y. Kawano *et al.*, Nuclear Fusion **45**, 318 (2005).

[21] M. N. Rosenbluth, S. V. Putvinski, and P. B. Parks, Nuclear Fusion **37**, 955 (1997).

[22] A. B. Rechester and M. N. Rosenbluth, Physical Review Letters **40**, 38 (1978).

[23] R. Yoshino and S. Tokuda, Nuclear Fusion **40**, 1293 (2000).

[24] P. Helander, L.-G. Eriksson, and F. Andersson, Physics of Plasmas **7**, 4106 (2000).

[25] F. Andersson, P. Helander, and L.-G. Eriksson, Physics of Plasmas **8**, 5221 (2001).

[26] L.-G. Eriksson and P. Helander, Computer Physics Communications **154**, 175 (2003).

[27] S. C. Chiu, M. N. Rosenbluth, R. W. Harvey, and V. S. Chan, Nuclear Fusion **38**, 1711 (1998).

[28] *Handbook of Mathematical Functions*, edited by M. Abramowitz and I. Stegun (Dover, New York, 1974).

[29] P. Helander, L.-G. Eriksson, and F. Andersson, Plasma Physics and Controlled Fusion **44**, B247 (2002).

[30] R. Jaspers, N. J. L. Cardozo, F. C. Schüller, K. H. Finken, T. Grewe, and G. Mank, Nuclear Fusion **36**, 367 (1996).

[31] J. R. Martín-Solís, R. Sánchez, and B. Esposito, Physics of Plasmas **7**, 3369 (2000).

[32] V. V. Plyusnin, V. Riccardo, R. Jaspers *et al.*, Nuclear Fusion **46**, 277 (2006).

[33] S. Putvinski, N. Fujisawa, D. Post, N. Putvinskaya, M. N. Rosenbluth, and J. Wesley, Journal of Nuclear Materials **241-243**, 316 (1997).

[34] L.-G. Eriksson, P. Helander, F. Andersson, D. Anderson, and M. Lisak, Physical Review Letters **92**, 205004:1 (2004).

[35] N. J. Fisch and M. D. Kruskal, Journal of Mathematical Physics **21**, 740 (1980).

[36] R. Beals, Journal of Mathematical Physics **22**, 954 (1981).

[37] H. A. Bethe, M. E. Rose, and L. P. Smith, Proceedings of the American Philosophical Society **78**, 573 (1938).

[38] R. D. Hazeltine and F. L. Waelbroeck, *The Framework of Plasma Physics* (Perseus Books, Reading, 1998).

[39] P. C. Clemmow and J. P. Dougherty, *Electrodynamics of Particles and Plasmas* (Addison-Wesley, London, 1969).

[40] H. Alfvén, Nature **150**, 405 (1942).

[41] G. Y. Fu and J. W. Van Dam, Physics of Fluids B **1**, 1949 (1989).

[42] K. Appert, R. Gruber, F. Troyon, and J. Vaclavik, Plasma Physics **24**, 1147 (1982).

[43] H. L. Berk, D. N. Borba, B. N. Breizman, S. D. Pinches, and S. E. Sharapov, Physical Review Letters **87**, 185002:1 (2001).

[44] S. Cauffman and R. Majeski, Review of Scientific Instruments **66**, 817 (1995).

[45] G. A. Cottrell and R. O. Dendy, Physical Review Letters **60**, 33 (1988).

[46] K. G. McClements, C. Hunt, R. O. Dendy, and G. A. Cottrell, Physical Review Letters **82**, 2099 (1999).

[47] M. Seki, M. Saigusa, M. Nemoto, K. Kusama, T. Tobita, M. Kuriyama, and K. Uchara, Physical Review Letters **62**, 1989 (1989).

[48] R. O. Dendy, C. N. Lashmore-Davies, K. G. McClements, and G. A. Cottrell, Physics of Plasmas **1**, 1918 (1994).

[49] T. Fülöp, Y. I. Kolesnichenko, M. Lisak, and D. Anderson, Nuclear Fusion **37**, 1281 (1997).

[50] B. Coppi, S. Cowley, R. Kulsrud, P. Detragiache, and F. Pegoraro, Physics of Fluids **29**, 4060 (1986).

[51] B. Coppi, Physics Letters A **172**, 439 (1993).

[52] B. Coppi, G. Penn, and C. Riconda, Annals of Physics **261**, 117 (1997).

[53] G. Penn, C. Riconda, and F. Rubini, Physics of Plasmas **5**, 2513 (1998).

[54] N. N. Gorelenkov and C. Z. Cheng, Nuclear Fusion **35**, 1743 (1995).

[55] Y. I. Kolesnichenko, T. Fülöp, M. Lisak, and D. Anderson, Nuclear Fusion **38**, 1871 (1998).

[56] T. Fülöp, M. Lisak, Y. I. Kolesnichenko, and D. Anderson, Physics of Plasmas **7**, 1479 (2000).

[57] N. N. Gorelenkov, C. Z. Cheng, and E. Fredrickson, Physics of Plasmas **9**, 3483 (2002).

[58] E. D. Fredrickson, N. Gorelenkov, C. Z. Cheng *et al.*, Physical Review Letters **87**, 145001:1 (2001).

[59] E. D. Fredrickson, N. N. Gorelenkov, and J. Menard, Physics of Plasmas **11**, 3653 (2004).

[60] L. C. Appel, R. J. Akers, T. Fülöp, R. Martin, and T. Pinfold, in *Proc. of the 31st European Physical Society Conference on Plasma Physics* (European Physical Society, London, 2004), Vol. 28G, p. P4.195.

[61] W. Heidbrink, E. Fredrickson, N. Gorelenkov, T. Rhodes, and M. V. Zeeland, Nuclear Fusion **46**, 324 (2006).

[62] N. Gorelenkov, E. Fredrickson, W. Heidbrink, N. Crocker, S. Kubota, and W. Peebles, Nuclear Fusion **46**, S933 (2006).

[63] N. N. Gorelenkov, E. D. Fredrickson, E. Belova, D. Gates, S. Kaye, and R. White, Nuclear Fusion **43**, 228 (2003).

[64] W. D. D'haeseleer, W. N. G. Hitchon, J. D. Callen, and J. L. Shohet, *Flux Coordinates and Magnetic Field Structure: A Guide to a Fundamental Tool of Plasma Theory* (Springer Verlag, Berlin, 1991).

[65] Y. I. Kolesnichenko, V. V. Parail, and G. V. Pereverzev, *Reviews of Plasma Physics* (Consultants Bureau, New York, 1992), Vol. 17, p. 1.

[66] H. Kimura, Y. Kusama, M. Saigusa *et al.*, Nuclear Fusion **38**, 1303 (1998).

[67] S. E. Sharapov, D. Testa, B. Alper *et al.*, Physics Letters A **289**, 127 (2001).

[68] R. Nazikian, G. J. Kramer, C. Z. Cheng, N. N. Gorelenkov, H. L. Berk, and S. E. Sharapov, Physical Review Letters **91**, 125003:1 (2003).

[69] M. A. V. Zeeland, G. J. Kramer, R. Nazikian, H. L. Berk, T. N. Carlstrom, and W. M. Solomon, Plasma Physics and Controlled Fusion **47**, L31 (2005).

[70] J. A. Snipes, N. Basse, C. Boswell *et al.*, Physics of Plasmas **12**, 056102:1 (2005).

[71] S. D. Pinches, R. J. Akers, L. C. Appel *et al.*, in *Proc. of the 21th International Conference on Fusion Energy 2006, Chengdu* (IAEA, Vienna, 2006), pp. EX/7–2Ra.

[72] S. E. Sharapov, B. Alper, H. L. Berk *et al.*, Physics of Plasmas **9**, 2027 (2002).

[73] A. Fukuyama and T. Akutsu, in *Proc. of the 19th International Conference on Fusion Energy 2002, Lyon* (IAEA, Vienna, 2003), pp. TH/P3–14.

[74] M. Takechi, A. Fukuyama, M. Ishikawa *et al.*, Physics of Plasmas **12**, 082509:1 (2005).

[75] M. Ishikawa, M. Takechi, K. Shinohara *et al.*, Nuclear Fusion **46**, S898 (2006).

[76] S. E. Sharapov, B. Alper, Y. F. Baranov *et al.*, Nuclear Fusion **46**, S868 (2006).

[77] F. Zonca, S. Briguglio, L. Chen, S. Dettrick, G. Fogaccia, D. Testa, and G. Vlad, Physics of Plasmas **9**, 4939 (2002).

[78] B. N. Breizman, H. L. Berk, M. S. Pekker, S. D. Pinches, and S. E. Sharapov, Physics of Plasmas **10**, 3649 (2003).

[79] H. L. Berk, J. W. van Dam, and D. M. Lindberg, Physics of Fluids B **4**, 1806 (1992).

[80] B. N. Breizman, M. S. Pekker, S. E. Sharapov, and JET EFDA contributors, Physics of Plasmas **12**, 112506:1 (2005).

[81] G. Y. Fu and H. L. Berk, Physics of Plasmas **13**, 052502:1 (2006).

[82] K. Gál, H. Smith, T. Fülöp, and P. Helander, in *Proc. of the 21th International Conference on Fusion Energy 2006, Chengdu* (IAEA, Vienna, 2006), pp. TH/P3–2.

[83] M. Porkolab, E. Edlund, L. Lin *et al.*, in *Proc. of the 21th International Conference on Fusion Energy 2006, Chengdu* (IAEA, Vienna, 2006), pp. EX/P6–16.

Included Papers A–G

Paper A

P. Helander, H. Smith, T. Fülöp, and L.-G. Eriksson, "Electron kinetics in a cooling plasma", Physics of Plasmas **11**, 5704 (2004).

Paper B

H. Smith, P. Helander, L.-G. Eriksson, and T. Fülöp, "Runaway electron generation in a cooling plasma", Physics of Plasmas **12**, 122505 (2005).

Paper C

H. Smith, P. Helander, L.-G. Eriksson, D. Anderson, M. Lisak, and F. Andersson, "Runaway electrons and the evolution of the plasma current in tokamak disruptions", Physics of Plasmas **13**, 102502 (2006).

Paper D

F. Andersson, P. Helander, D. Anderson, H. Smith, and M. Lisak, "Approximate solutions of two-way diffusion equations", Physical Review E **65**, 036502 (2002).

Paper E

F. Andersson, H. Smith, D. Anderson, P. Helander, and M. Lisak, "Effects of backscattering on one-dimensional electron beam transport", Nuclear Science and Engineering **142**, 150 (2002).

Paper F

H. Smith, T. Fülöp, M. Lisak, and D. Anderson, "Localization of compressional Alfvén eigenmodes in spherical tori", Physics of Plasmas **10**, 1437 (2003).

Paper G

H. Smith, B. N. Breizman, M. Lisak, and D. Anderson, "Non-linearly driven second harmonics of Alfvén cascades", Physics of Plasmas **13**, 042504 (2006).

Errata

- There is a v missing in Eq. 3.1. It should read

$$\frac{\partial f}{\partial t} = \frac{1}{2v^2}\frac{\partial}{\partial v}v^3\left(\nu_{\rm s}^{\rm ee} f + \nu_{\parallel}^{\rm ee} v\frac{\partial f}{\partial v}\right) + \frac{1}{v^2}\frac{\partial}{\partial v}\left(\nu^{ez} v^3 f\right)$$

- Below Eq. (2.30), the expression should be

$$\varphi = (1 + 1.46\epsilon^{1/2} + 1.72\epsilon)^{-1}$$

- In the text before Eq. (8.3) on page 59 it should say: "$V = \dot{\Phi}_1/c$ and $\mathbf{A}_\perp = \nabla\Psi_1 \times \mathbf{b}_0$", and Eq. (8.3) should read

$$\mathbf{v}_1 = c\frac{\mathbf{E}\times\mathbf{B}_0}{B_0^2} = \frac{\mathbf{b}_0}{B_0}\times\nabla\dot{\Phi}_1 + \frac{1}{B_0}\nabla_\perp\dot{\Psi}_1.$$

- The third line from the bottom of page 60 should start with: $\mathbf{B}_1 \propto e^{-i\omega t}$, $\mathbf{B}_2 \propto e^{-2i\omega t}\ldots$

- On the sixth line below Eq. (8.11) on page 62 it should read: "Hence, at low Q the nonlinearity of the momentum balance equation gives the most prominent contribution to ρ_2. On the other hand, when Q is high, as in Fig. 8.2b ..."

- In Fig. 3 of Paper E the top figure is (b) and the bottom one is (a).